



## Assimilation of POLDER observations to estimate aerosol emissions

Athanasios Tsikerdekis<sup>1,2,a</sup>, Otto P. Hasekamp<sup>1</sup>, Nick A. J. Schutgens<sup>2</sup>, and Qirui Zhong<sup>2</sup>

<sup>1</sup>SRON Netherlands Institute for Space Research, Leiden, the Netherlands

<sup>2</sup>Department of Earth Sciences, Vrije Universiteit Amsterdam, Amsterdam, the Netherlands

<sup>a</sup>now at: Royal Netherlands Meteorological Institute (KNMI), De Bilt, the Netherlands

**Correspondence:** Otto P. Hasekamp (o.p.hasekamp@sron.nl) and Athanasios Tsikerdekis (thanos.tsikerdekis@knmi.nl)

Received: 26 January 2023 – Discussion started: 22 February 2023

Revised: 21 June 2023 – Accepted: 6 July 2023 – Published: 29 August 2023

**Abstract.** We apply a local ensemble transform Kalman smoother (LETKS) in combination with the global aerosol–climate model ECHAM–HAM to estimate aerosol emissions from POLDER-3/PARASOL (POLARization and Directionality of the Earth’s Reflectances) observations for the year 2006. We assimilate aerosol optical depth at 550 nm ( $AOD_{550}$ ), the Ångström exponent at 550 and 865 nm ( $AE_{550-865}$ ), and single-scattering albedo at 550 nm ( $SSA_{550}$ ) in order to improve modeled aerosol mass, size and absorption simultaneously. The new global aerosol emissions increase to  $1419 \text{ Tg yr}^{-1}$  (+28 %) for dust,  $1850 \text{ Tg yr}^{-1}$  (+75 %) for sea salt,  $215 \text{ Tg yr}^{-1}$  (+143 %) for organic aerosol and  $13.3 \text{ Tg yr}^{-1}$  (+75 %) for black carbon, while the sulfur dioxide emissions increase to  $198 \text{ Tg yr}^{-1}$  (+42 %) and the total deposition of sulfates to  $293 \text{ Tg yr}^{-1}$  (+39 %). Organic and black carbon emissions are much higher than their prior values from bottom-up inventories, with a stronger increase in biomass burning sources (+193 % and +90 %) than in anthropogenic sources (115 % and 70 %). The evaluation of the experiments with POLDER (assimilated) and AERONET as well as MODIS Dark Target (independent) observations shows a clear improvement compared with the ECHAM–HAM control run. Specifically based on AERONET, the global mean error in  $AOD_{550}$  improves from  $-0.094$  to  $-0.006$ , while absorption aerosol optical depth at 550 nm ( $AAOD_{550}$ ) improves from  $-0.009$  to  $-0.004$  after the assimilation. A smaller improvement is also observed in the  $AE_{550-865}$  mean absolute error (from 0.428 to 0.393), with a considerably higher improvement over isolated island sites at the ocean. The new dust emissions are closer to the ensemble median of AEROCOM I, AEROCOM III and CMIP5 as well as some of the previous assimilation studies. The new sea salt emissions have become closer to the reported emissions from previous studies. Indications of a missing fraction of coarse dust and sea salt particles are discussed. The biomass burning changes (based on POLDER) can be used as alternative biomass burning scaling factors for the Global Fire Assimilation System (GFAS) inventory distinctively estimated for organic carbon (2.93) and black carbon (1.90) instead of the recommended scaling of 3.4 (Kaiser et al., 2012). The estimated emissions are highly sensitive to the relative humidity due to aerosol water uptake, especially in the case of sulfates. We found that ECHAM–HAM, like most of the global climate models (GCMs) that participated in AEROCOM and CMIP6, overestimated the relative humidity compared with ERA5 and as a result the water uptake by aerosols, assuming the kappa values are not underestimated. If we use the ERA5 relative humidity, sulfate emissions must be further increased, as modeled sulfate AOD is lowered. Specifically, over East Asia, the lower AOD can be attributed to the underestimated precipitation and the lack of simulated nitrates in the model.

## 1 Introduction

A prominent uncertain component in aerosol modeling is the aerosol emissions. The uncertainty in aerosol emissions enhances the unpredictability in the simulated aerosol concentration and optical properties (Textor et al., 2007) as well as in the aerosol radiative effect and forcing (Myhre et al., 2013; Yoshioka et al., 2019). A bottom-up estimate of anthropogenic aerosol emissions usually comes from the integration of known sources of information across different economic sectors, such as power, industry, transport and residential (Zhang et al., 2009). These bottom-up techniques are very useful since they provide a first-guess estimate of aerosol emissions, but emission differences in source attribution (power, industry, residential) may lead to very different simulated aerosol concentrations (Saikawa et al., 2017).

Natural aerosol emissions like dust and sea salt are estimated in aerosol models through different schemes by using wind speed as well as land or ocean characteristics (Grythe et al., 2014; Long et al., 2011; Tegen et al., 2002). A large fraction of the natural emissions diversity can be attributed to differences in the modeling approaches. Emission schemes can differ in the parameterization of source strength as a function of wind (Grythe et al., 2014; Textor et al., 2007), the simulated winds themselves (Textor et al., 2007), the simulated size spectrum of the emitted particles (Kok et al., 2021; Textor et al., 2006), the simulated size grouping in each model (e.g., modes or bins) (Gliß et al., 2021) and the implementation of spatial filters where dust emission sources can change dynamically based on vegetation (Wu et al., 2020). Also, large differences in the simulated natural emissions can emerge by simply using a different horizontal resolution in the same model (Guelle et al., 2001; Laurent et al., 2008). In addition, the physically relevant scale (from 1 m to several km) where dust emissions can vary is not captured by the current horizontal resolution of global climate models (Kok et al., 2021).

Emissions from biomass burning are estimated based on satellite measurements that are related to burned area and that use emission factors to convert the burned dry matter into emissions of aerosol and gas species (Global Fire Emissions Database v4 (GFED4); Van der Werf et al., 2017), active fire count (Fire INventory from NCAR v1.5 (FINN1.5); Wiedinmyer et al., 2011), or fire radiative power (Quick Fire Emissions Dataset v2.4 (QFED2.4); Darmenov and da Silva, 2015; Fire Energetics and Emissions Research version v1.0 (FEER1.0); Ichoku and Ellison, 2014; and Global Fire Assimilation System (GFAS); Kaiser et al., 2012). It has been shown that different emission factors may contribute to the diversity between these emission inventories, but differences in the dry matter have also been reported for North America fires (Carter et al., 2020), which is one of the main reasons that the fire detection and/or fire burden area inventories do not align with fire radiative power inventories (Van der Werf et al., 2017). In addition, strong interannual differences and

regional diversity are observed between the datasets, with a fairly good agreement over the Amazon and a quite high disagreement over Africa and boreal North America (Carter et al., 2020).

The global dust emissions relative diversity (usually quantified as the ratio of the standard deviation to the mean) (Schutgens et al., 2020) for the multi-model ensemble of CMIP5 is 87 % (Wu et al., 2020), and for AEROCOM I it is 73 % (Huneus et al., 2011), while for several simulations from a single model with diverse emission scheme settings it is 61 % (Miller et al., 2006). The sea salt emission relative diversity is 97 % based on several different sea salt emission functions (Grythe et al., 2014) for global estimates within the range of 1200 to 20000 Tg yr<sup>-1</sup> as proposed by Lewis and Schwartz (2004). The emission relative diversity from biomass burning based on six emission datasets is 76 % for organic carbon and 82 % for black carbon (Pan et al., 2020). Consequently, the global emissions of aerosol from natural sources, such as deserts (dust), oceans (sea salt) and non-anthropogenic biomass burning (organic and black carbon – OC and BC), are at least higher than 60 %; hence there is a lot of room for improvement.

The differences between various anthropogenic emission inventories is considerably lower than the differences between various natural emission estimates for aerosol. In Lee et al. (2013), lower OC and BC uncertainty was found for fossil fuel compared with biomass burning emissions as well as lower SO<sub>2</sub> uncertainty for fossil fuel compared with volcanic emissions. The emission diversity estimated by multiple anthropogenic emission inventories, as the ratio of the highest to the lowest anthropogenic global emissions, showed that it is lower than 20 % for BC and NO<sub>x</sub> and lower than 42 % for SO<sub>2</sub> after the year 2000 (Granier et al., 2011). The relative diversity of anthropogenic aerosol and aerosol precursor emissions over large areas is significantly lower, but note that these different emissions inventories are constructed using very similar information and methods; therefore they are not independent from each other (Granier et al., 2011). Based on four emission inventories over eastern China for 2006, the emissions relative diversity (using the mean in the denominator) of SO<sub>2</sub>, ammonia (NH<sub>3</sub>), OC and BC is 5 %, 18 %, 12 % and 16 %, respectively (Chang et al., 2015). Note that this diversity is based on yearly means; hence the day-to-day variability and relative diversity among these emission inventories can be higher. Further, the sector attribution of emissions can be quite different in each dataset, which can affect the uncertainty in emissions on the regional level (Saikawa et al., 2017).

These high emissions differences for modeled fluxes of dust and sea salt as well as differences in fluxes in emission inventories for the other aerosol species led to the popularization of the top-down method that combines simulated aerosol information from a model and retrieved aerosol information from satellites (Chen et al., 2018, 2019, 2022; Dubovik et al., 2008; Escribano et al., 2017; Huneus et al.,

2012; Jin et al., 2019; Pope et al., 2016; Schutgens et al., 2012; Sekiyama et al., 2010; X. Xu et al., 2013). The simulated aerosol state in the model is produced using background emissions which are either prescribed from emission inventories (anthropogenic aerosols and biomass burning) or interactively calculated through emission schemes (dust and sea salt aerosols). In addition, the uncertainty in the assimilated observations and the uncertainty in the background emissions need to be specified.

Most of the abovementioned studies have estimated new emissions based on the assimilation of aerosol optical depth (AOD), some studies have also included the Ångström exponent (AE), while very few studies have assimilated absorption observations like absorption aerosol optical depth (AAOD) or single-scattering albedo (SSA) (Zhang et al., 2015; Chen et al., 2018, 2019, 2022). By not including observations of measurements related to size and absorption, the estimated emission may be misrepresented as it has been shown for the estimated aerosol mixing ratio in Tsikerdekis et al. (2021), where several data assimilation experiments were conducted with different combinations of observations from the POLDER (POLARization and Directionality of the Earth's Reflectances) instrument. The multi-wavelength and multi-viewing-angle photopolarimetric measurements of POLDER contain more information about the scattered solar radiation compared with single-viewing measurements (Hasekamp and Landgraf, 2007; Mishchenko and Travis, 1997); hence POLDER is an ideal tool for obtaining accurate aerosol microphysical and optical properties, which can potentially provide a more accurate estimation of emissions, as suggested in Schutgens et al. (2021).

Although aerosol emissions are critically uncertain, other factors can affect the uncertainty in modeled aerosol concentration and optical properties. One of these factors is the aerosol water uptake in models that can considerably increase the simulated AOD diversity (Gliß et al., 2021). The misrepresentation of water uptake can have a huge impact, since the condensed water over dry aerosol particles may contribute up to 70 % of the total AOD globally (K. Zhang et al., 2012). During the AEROCOM I phase, substantial diversity among the model was attributed to differences in the modeled water uptake (Kinne et al., 2006). A recent study has evaluated the scattering enhancement factor of 10 Earth system models based on 22 ground-based in situ measurements (Burgos et al., 2020). The scattering enhancement factor for a certain wavelength ( $\lambda$ ) is the ratio of the light scattering coefficient under wet (relative humidity (RH) = 85 %) to dry (RH = 40 %) conditions, which describes the increase in aerosol scattering due to the wet growth of particles under different RH conditions. The results showed that the models tend to overestimate the scattering enhancement factor as an ensemble mean by 15 %, though the differences from model to model were quite substantial. The inter-model differences were attributed to different assumptions in kappa and contrasting growth under low-RH (RH < 40 %) conditions be-

tween the models. Further, it was suggested that lower kappa values should be used in the models for organics and sea salt, and considerable differences were found between the models for the light scattering enhancement factor under relatively dry conditions (RH < 40 %). Although this study is very insightful, the discretization of the scattering enhancement factor based on RH could correspond to a diverse aerosol load for each model. The low- and high-RH conditions may have occurred at different times and on different dates for every model and for the observations. In our study we assume that kappa is correct for our experiments, and we investigate how a biased RH may influence aerosol water growth and their optical properties as well as estimated aerosol emissions by the data assimilation system.

The effect of a biased RH, which can dramatically affect the simulated aerosol optical properties, has so far received little attention. The current horizontal resolution of global climate models (GCMs), which for the majority of AEROCOM III and CMIP6 models is between 1° and 2° (Gliß et al., 2021; Z. Xu et al., 2021), cannot resolve humidity's small-scale processes; thus they are parameterized through cloud schemes (Lin, 2014). Because of this, biases in the simulated humidity can accumulate in GCMs. The specific humidity of the CMIP5 ensemble is overestimated over mid-latitudes throughout the troposphere when compared with the Atmospheric Infrared Sounder (AIRS) (Tian et al., 2013). Further, the majority of the CMIP6 model ensemble (12 out of 18) overestimates relative humidity at 850 hPa in all seasons compared with ERA5 (Z. Xu et al., 2021).

In the present study we estimate the aerosol emissions of dust (DU), sea salt (SS), organic carbon (OC), black carbon (BC), sulfates (SO<sub>4</sub>) and precursor gas emissions for sulfates like sulfur dioxide (SO<sub>2</sub>) and dimethyl sulfide (DMS) for the year 2006. Our method implements a local ensemble transform Kalman smoother (LETKS), which has been introduced in our preceding work (Tsikerdekis et al., 2022a). It combines POLDER observations, which were retrieved by the algorithm developed at the Netherlands Institute for Space Research (SRON), with the aerosol information simulated by ECHAM-HAM. We assimilate AOD<sub>550</sub>, AE<sub>550–865</sub> and SSA<sub>550</sub> in order to simultaneously account for the correction of aerosol mass, size and absorption (Tsikerdekis et al., 2021). In addition, we conduct sensitivity and data assimilation experiments using the relative humidity of ERA5 (instead of ECHAM-HAM) for the water uptake process to quantify the effect it has on aerosol optical properties and the estimated emissions. Section 2 presents the retrieved observations from POLDER and the model ECHAM-HAM. The observations and emissions uncertainties are discussed. Section 3 briefly describes the LETKS and provides an overview of our experiments. Section 4 includes the evaluation results of our experiments against POLDER and independent observations (AERONET and MODIS) as well as the new estimated emissions along with the reported emissions from pre-

vious studies. In addition, we quantify the effect of a biased high RH on aerosol optical properties and emissions.

## 2 Data

### 2.1 Aerosol observations (POLDER)

POLDER-3 (POLarization and Directionality of the Earth's Reflectances) is an instrument that can measure light intensity and polarization properties from up to 16 viewing angles and from multiple wavelengths (0.44 to 1.02  $\mu\text{m}$ ). In addition, the multi-angle multi-wavelength photopolarimetric measurements have the ability to differentiate scattering of cloud droplets from aerosol particles; thus the exclusion of cloud-contaminated pixels is possible (Stap et al., 2015). The instrument was part of the Polarization and Anisotropy of Reflectances for Atmospheric Sciences coupled with Observations from a Lidar (PARASOL) micro-satellite, which was active from 2004 to 2013.

The aerosol products derived from POLDER observations that were used in this study were retrieved by an algorithm developed at SRON (Netherlands Institute for Space Research), which fits a radiative transfer model (Hasekamp and Landgraf, 2005; Schepers et al., 2014) to the multi-angle photopolarimetric measurements of POLDER to derive aerosol optical properties corresponding to a bimodal aerosol size distribution. We use the global bimodal product, which is the only product available globally, but note that a regional 10-mode product achieved higher accuracy for AOD and a similar performance for SSA when compared with AERONET for retrievals over land (Fu and Hasekamp, 2018). The retrieved properties for a fine- and coarse-mode particle are the effective radius, the effective variance and the column number concentration as well as the real and imaginary part of the refractive index for each mode (Hasekamp et al., 2011, 2019; Lacagnina et al., 2015; Wu et al., 2015). By using the abovementioned aerosol parameters for the two modes, we can calculate the aerosol optical depth (AOD), the Ångström exponent (AE), the absorption aerosol optical depth (AAOD) and the single-scattering albedo (SSA). The aerosol optical properties of POLDER retrievals demonstrate good agreement with either ground-based (AERONET) or satellite (Ozone Monitoring Instrument; OMI) retrievals for the year 2006 (Hasekamp et al., 2011; Lacagnina et al., 2015, 2017; Stap et al., 2015).

In the present study, aggregated ( $1^\circ \times 1^\circ$ ) POLDER data are used in the assimilation for the year 2006. The year 2006 was selected based on the availability of POLDER aerosol products from the SRON retrieval algorithm. POLDER uncertainty for each assimilated observable was estimated for several POLDER AOD<sub>550</sub> bins based on an AERONET evaluation and is presented in Appendix A. Note that POLDER AE<sub>550–865</sub> over the Sahara is biased high based on AERONET; thus these observations were not assimilated (see Appendix A). A more detailed description of the use of

POLDER data in our assimilation system can be found in Tsikerdekis et al. (2021), and details on the SRON POLDER retrieval algorithm can be found in Fu et al. (2020) and Fu and Hasekamp (2018).

### 2.2 Aerosol model (ECHAM6–HAM2)

The aerosol–climate model ECHAM6–HAM2 (hereafter called ECHAM–HAM) is used to simulate the meteorological and aerosol state of the atmosphere. The model consists of two parts, the general circulation model ECHAM6, developed at the Max Planck Institute for Meteorology (MPI-M) in Hamburg, Germany (Stevens et al., 2013), and the second version of the Hamburg Aerosol Model (HAM2) (Stier et al., 2005; Tegen et al., 2019; K. Zhang et al., 2012). Aerosols are simulated in seven unimodal lognormal particle size distributions (modes); four of them are the hydrophilic nucleation, Aitken, accumulation and coarse, while three of them are the hydrophobic Aitken, accumulation and coarse. Each mode may contain one or more (internally mixed) aerosol species, namely dust (DU), sea salt (SS), organic carbon (OC), black carbon (BC) and sulfates (SO<sub>4</sub>) (Vignati et al., 2004). Currently the model does not simulate aerosol nitrates. The cloud and aerosol optical properties are computed using Mie theory and are derived from lookup tables (Tegen et al., 2019) using the prognostic concentrations of aerosol tracers (Schultz et al., 2018).

All aerosol species are emitted, transported and deposited, and they take part in aerosol–radiation interactions (scattering and absorption) as well as in aerosol microphysical processes (e.g., nucleation, coagulation, aerosol water uptake and cloud activation) (Schutgens and Stier, 2014; K. Zhang et al., 2012). The natural aerosol types (DU, SS) are introduced into the atmosphere by utilizing the simulated information of wind and certain surface and ocean characteristics. Other aerosol species (OC, BC) or aerosol precursor gases (SO<sub>2</sub>, DMS) that are emitted from both natural (biomass burning or biogenic emissions) and anthropogenic sources (e.g., industry and transport) use predefined emission inventories (K. Zhang et al., 2012). Specifically, anthropogenic emissions are derived from 14 different sectors. Each sector may include one or more aerosol types or aerosol precursors (Schultz et al., 2018; Tegen et al., 2019). A more detailed description of the model is available in our preceding work (Tsikerdekis et al., 2021, 2022a).

Aerosol water uptake is the process of condensing water vapor on the surface of aerosol particles. This process affects the aerosol's size, deposition, atmospheric lifetime and optical properties. Thus, it is crucial to simulate aerosol water uptake accurately in aerosol models. In ECHAM–HAM water uptake is simulated by a semi-empirical water uptake scheme (O'Donnell et al., 2011) that approximates the enhancement of particle size (growth factor; gf) based on Petters and Kreidenweis (2007). Based on this scheme the growth of aerosol particles depends on the relative humidity (RH); the dry par-

title radius ( $D_p$ ); the kappa parameter ( $\kappa$ ), which is distinctive for each aerosol species and which determines its hygroscopicity; and the Kelvin term ( $A$ ), which is a temperature-dependent constant (O'Donnell et al., 2011). In order to enhance computational efficiency, this equation is solved offline and is organized in lookup tables where the aerosol growth factor can be determined for specific RH,  $D_p$ ,  $k$  and  $A$  conditions in each grid cell of the model. Kappa expresses the volume of water that is associated with a unit volume of dry particles (Petters and Kreidenweis, 2013), and the higher it gets, the more soluble the aerosol species is. In ECHAM–HAM the kappa is fixed for each species. The kappa specifically for SS, SO<sub>4</sub> and OC is equal to 1.00, 0.60 and 0.06, respectively. DU and BC are considered insoluble ( $\kappa = 0$ ). The most decisive parameter of the above, which influences the growth factor of soluble particles (high  $\kappa$ ) the most, is RH. Hence, in this study we conduct experiments where RH from ERA5 is explicitly used for the water uptake of aerosols in ECHAM–HAM to quantify its effect on the simulated aerosol optical properties. Further, this option is adopted in a data assimilation experiment to quantify the effect of RH on aerosol emission estimation.

### 3 Methods

#### 3.1 The local ensemble transform Kalman smoother

The local ensemble transform Kalman smoother (LETKS) is used to estimate aerosol emission. This method was previously used by Schutgens et al. (2012) for aerosol emission estimation and earlier for CO<sub>2</sub> emission estimation (Bruhwiler et al., 2005; Peters et al., 2005; and Feng et al., 2009). A detailed description of LETKS can be found in Tsikerdekis et al. (2022) where the method and the code were tested for aerosol emission estimation using SPEXone synthetic measurements in observing system simulation experiments (OSSEs). Here the main components of the method are discussed.

The system estimates perturbation to the background emissions and assumes that these perturbations remain constant over 2 d. The emission perturbations are estimated using assimilation cycles, where each cycle consists of a background and an analysis step. The background step produces the required background information based on an 8 d ( $\Delta T_b$ ) forward simulation of ECHAM–HAM driven by a priori (“background”) emissions. The analysis step assimilates all the available POLDER observations within the last 2 d ( $\Delta T_s$ ) of the forward simulation and estimates the “analysis” emissions for the last 6 d ( $\Delta T_a = \Delta T_b - \Delta T_s$ ) of the forward simulation.

At the end of each assimilation cycle the estimated analysis emissions of the previous cycle serve as background emissions for the next cycle, time is shifted forward equal to  $\Delta T_s$  days, and the background and analysis steps are repeated. Note that with this setup several assimilation cycles overlap

in time; thus the estimated emissions (estimated in batches of 2 d) are affected by observations of the current and subsequent days. Specifically, the emissions of a day may be affected by observations of the same day and of the 5 subsequent days. This iterative design ensures that observations close to the sources along with observations away from the sources (e.g., an aerosol plume created by particles emitted several days earlier) will both be used to correct the emissions.

The assumed background emissions are uncertain. The uncertainty in the emissions is represented with an ensemble of 32 simulations where emissions are perturbed. The perturbation is conducted by multiplying the emissions by spatially correlated perturbations (see Sect. 3.2 on Tsikerdekis et al., 2021). The spatial correlation length scale of the perturbations is approximately 25° omnidirectionally, except for DU perturbations over the Sahara where the spatial correlation length is zero (perturbations from grid to grid are uncorrelated). The zero spatial correlation length for DU over the Sahara was chosen after conducting several data assimilation experiments with different correlation length values and evaluating them in terms of AOD<sub>550</sub> (not shown). Each perturbation set is uniquely generated for every perturbed parameter and ensemble member. In each grid cell, the mean of the background distribution of the emission scaling factor for the first cycle is equal to 1, while for all subsequent cycles the mean is set equal to the analysis distribution mean of the previous cycle (see prior correction subsection in Tsikerdekis et al., 2022a). In each grid cell, the standard deviation of the background distribution, which represents the uncertainty in the emissions, is distinct for each perturbed parameter and is further discussed in Appendix B.

New emission estimates are obtained by estimating scaling factors based on the assimilated observations by solving the following Kalman filter equations:

$$\mathbf{x}_a = \mathbf{x}_b + \mathbf{P}_a \cdot \mathbf{H}^T \cdot \mathbf{R}^{-1} \cdot (\mathbf{y} - \mathbf{H} \cdot \mathbf{x}_b), \quad (1)$$

$$\mathbf{P}_a = (\mathbf{I} + \mathbf{P}_b \cdot \mathbf{H}^T \cdot \mathbf{R}^{-1} \cdot \mathbf{H})^{-1} \cdot \mathbf{P}_b, \quad (2)$$

where  $\mathbf{x}_b$  is the background state vector and includes emission perturbations for each species (DU, SS, OC, BC and SO<sub>4</sub>). Different perturbations are used for each optically relevant mode (Aitken, accumulation, coarse) and for biomass burning (BB) or fossil fuel (FF) contributions. Specifically, the emissions that are distinctively perturbed and estimated (11 in total) by the assimilation system are shown in Table 1. The perturbation of sulfate precursor gasses (SO<sub>2</sub> and DMS) used the same perturbations as SO<sub>4</sub>.  $\mathbf{x}_a$  is the analysis state vector, containing the retrieved emission scaling factors based on the assimilated observations ( $\mathbf{y}$ ).  $\mathbf{P}_b$  and  $\mathbf{P}_a$  are the covariance matrices corresponding to the background and analysis state vector, respectively. The observational uncertainties are represented by the error covariance matrix  $\mathbf{R}$ . We assume  $\mathbf{R}$  to be diagonal (i.e., correlations between observational errors are always assumed to be zero). The observation

**Table 1.** Emission types that are distinctively perturbed and estimated (state vector) by the assimilation system. Fossil fuel refers to all emissions except biomass burning, which to a large extent includes mainly fossil fuel emissions but also other natural emissions like biogenic emissions. Biomass burning emissions include both natural and anthropogenic-induced fires. SO<sub>2</sub>, DMS and SO<sub>4</sub> share the same perturbations but are distinctively defined for biomass burning and fossil fuel. The sulfates in the atmosphere are mainly produced by emitted SO<sub>2</sub>, followed by DMS. Direct emissions of SO<sub>4</sub> are modeled as 2.5 % of the SO<sub>2</sub> emissions.

Species	Mode	Hygroscopicity	Sector
DU	Accumulation	Insoluble	–
DU	Coarse	Insoluble	–
SS	Accumulation	Soluble	–
OC	Aitken	Insoluble	Biomass burning
OC	Accumulation	Soluble	Biomass burning
OC	Aitken	Insoluble	Biomass burning
OC	Aitken + accumulation	Insoluble	Fossil fuel
BC	Aitken	Insoluble	Biomass burning
BC	Aitken	Insoluble	Fossil fuel
SO <sub>2</sub> , DMS, SO <sub>4</sub>	Aitken + accumulation + coarse	Soluble	Biomass burning
SO <sub>2</sub> , DMS, SO <sub>4</sub>	Aitken + accumulation + coarse	Soluble	Fossil fuel

**Table 2.** Experiments overview.

Experiment	Assimilation	Resolution	RH for water uptake
CTL <sub>ECHAM</sub>	–	1.875° × 1.875°	ECHAM–HAM
DAS <sub>ECHAM</sub>	POLDER AOD, AE, SSA	1.875° × 1.875°	ECHAM–HAM
CTL <sub>ERA5</sub>	–	1.875° × 1.875°	ERA5
DAS <sub>ERA5</sub>	POLDER AOD, AE, SSA	1.875° × 1.875°	ERA5
RES <sub>LOW</sub>	–	3.75° × 3.75°	ECHAM–HAM

operator  $H$  translates the emission perturbations ( $\mathbf{x}$ ) into the simulated observations ( $H \cdot \mathbf{x}$ ), and it is entirely handled by the model (emission, transport, deposition, aerosol processes and optical property code).  $T$  stands for the matrix transpose operator.

### 3.2 Experimental setup

All experiments are conducted using the model ECHAM–HAM for the year 2006. The experiments use 31 vertical sigma-hybrid levels from the surface to up to 10 hPa (troposphere-only simulations) and a T63 horizontal resolution of 1.875° × 1.875° and are nudged to ERA5 surface pressure as well as to vorticity, divergence and temperature for all vertical levels. A list of selected meteorological and aerosol options used for the experiments is presented in Table S1 in the Supplement.

CTL<sub>ECHAM</sub> is an ECHAM–HAM run without data assimilation and with default settings, while DAS<sub>ECHAM</sub> is a data assimilation experiment where the emissions are optimized based on measurements by POLDER. In addition, we conducted an experiment with an identical setup to CTL<sub>ECHAM</sub> but with lower horizontal resolution (T31; 3.75° × 3.75°).

CTL<sub>ERA5</sub> quantifies the effect of the underestimated relative humidity on aerosol optical properties in ECHAM compared with ERA5. CTL<sub>ERA5</sub> uses the relative humidity of

ERA5 for aerosol water uptake. Note that this modification affects only the simulated aerosol optical properties in ECHAM–HAM, while the simulated water cycle (precipitation and evaporation) of the model remains unaltered. A data assimilation experiment based on this new CTL<sub>ERA5</sub> setup, named DAS<sub>ERA5</sub>, was conducted in order to quantify the effect of the overestimated relative humidity profile on the aerosol emission estimation.

## 4 Results

### 4.1 Evaluating model fields with POLDER, AERONET and MODIS observations

All experiments were evaluated against the assimilated observations (POLDER) and independent observations (AERONET and MODIS). In both cases there is a significant improvement in all the aerosol optical properties in the DAS<sub>ECHAM</sub> experiment, except for AE<sub>550–865</sub> over some land areas where the error increases. This can possibly be attributed to the relatively high observational uncertainty for AE<sub>550–865</sub> (Fig. A1).

In Fig. 1 the experiments CTL<sub>ECHAM</sub> and DAS<sub>ECHAM</sub> are compared to the assimilated POLDER observations for the year 2006. CTL<sub>ECHAM</sub> exhibits a strong underestimation in AOD over the biomass burning regions over the tropics (the

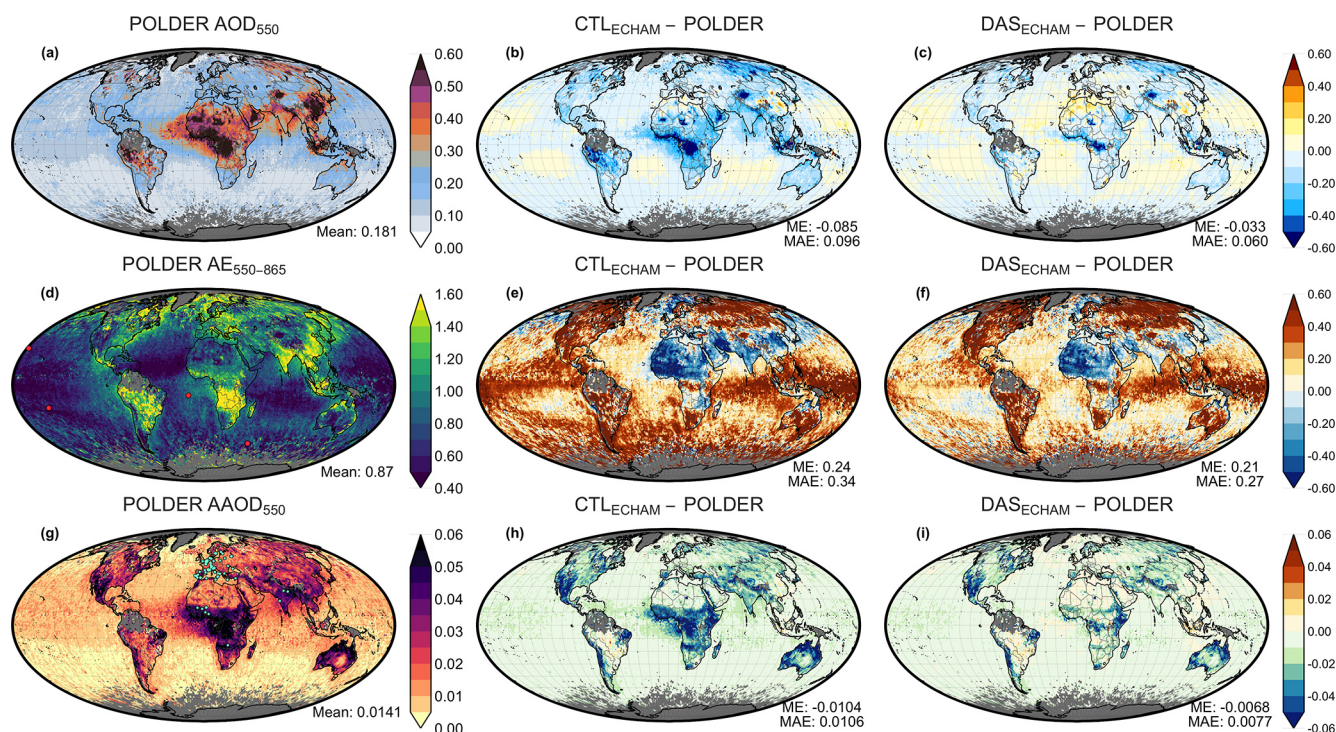


**Figure 1.** An evaluation of  $CTLECHAM$  and  $DASECHAM$  experiments, based on POLDER for the year 2006. The first column depicts POLDER (a)  $AOD_{550}$ , (b)  $AE_{550-865}$  and (c)  $AAOD_{550}$ , while the second and third columns display the differences between  $CTLECHAM - POLDER$  and  $DASECHAM - POLDER$ , respectively. The global mean, global mean error (ME) and global mean absolute error (MAE) are depicted in the bottom-right corner of each plot. The points in panels (d) and (g) depict AERONET stations used for the plots of Figs. 3 and 4, respectively.

Amazon, central Africa and Indonesia) and Siberia that are dominated by organic and black carbon aerosols, as well as over arid environments dominated by dust (the Sahara, the Middle East and the Taklimakan and Gobi deserts).  $AOD_{550}$  is overestimated over southeastern China, where the aerosol load is very high (POLDER  $AOD_{550}$  is higher than 0.6) and composed mostly of sulfates, as well as over open water bodies, where the aerosol load is low and dominated by sea salt. The  $CTLECHAM$   $AOD_{550}$  per species along with the optical depth due to condensed water on the surface of aerosol particles (WAT) are depicted in Fig. S1 in the Supplement. The assimilation of POLDER observations ( $DASECHAM$ ) reduces the  $AOD_{550}$  global mean error (ME) from  $-0.08$  to  $-0.03$  and the mean absolute error (MAE) from 0.10 to 0.06, which shows that ECHAM–HAM can match the observations with adjusted emissions better. Note that the local improvement of  $AOD_{550}$  for certain regions is even greater.

The  $AE_{550-865}$  is a good proxy for aerosol size. High and low values of  $AE_{550-865}$  relate to an aerosol load with more fine and more coarse particles, respectively. POLDER  $AE_{550-865}$  is high over biomass burning and highly polluted regions, dominated mainly by OC, BC and  $SO_4$ , while it is low over the ocean and deserts where the aerosol load is primarily composed of DU and SS (Fig. 1d). In  $CTLECHAM$ ,  $AE_{550-865}$  is underestimated over the Sahara, the Middle East

and eastern China, while it is overestimated over the ocean, Siberia, and North and South America. The estimated emissions by  $DASECHAM$  improve the  $AE_{550-865}$  difference over the ocean, and there is a significant improvement over China. The remaining high differences in  $AE_{550-865}$  over land can be attributed to the high uncertainty in POLDER  $AE_{550-865}$  over land. In Fig. S2 the yearly mean uncertainty in POLDER is depicted along with the MAE of the 3-hourly differences in  $CTLECHAM - POLDER$  and  $DASECHAM - POLDER$ . The remaining MAEs of the 3-hourly differences in  $DASECHAM$  (Fig. S2c) are on the same level as the POLDER uncertainty (Fig. S2a), which means that POLDER  $AE_{550-865}$  over land is too uncertain to adjust emissions further. Additionally, sensitivity studies have shown that even when the biomass-burning-emitted particle size is altered aggressively in ECHAM–HAM, AE is not affected much (Zhong et al., 2022), which indicates that the emission changes may be less sensitive to the assimilation of  $AE_{550-865}$  compared to  $AOD_{550}$ . The global MAE for  $AE_{550-865}$  is reduced from 0.34 in  $CTLECHAM$  to 0.27 in  $DASECHAM$ .

$AAOD_{550}$  is highly correlated with the BC aerosol load, which is the species that contributes up to 80 % of the total absorption globally, followed by DU (16 %) and OC (4 %) (Fig. S3). POLDER  $AAOD_{550}$  peaks over tropical Africa and Sahel, where large biomass burning fires are active during

the fire (dry) season. Fairly high values of absorption are also observed over the Amazon Basin for the same reason. Further, high  $\text{AAOD}_{550}$  values are depicted over the northern and western coastline of Australia, which is probably a product of retrieval errors. Medium values of  $\text{AAOD}_{550}$  that are related to anthropogenic emissions are visible over the eastern United States, Europe and eastern China. POLDER also depicts high  $\text{AAOD}_{550}$  values over high-altitude regions (Schutgens et al., 2021), like the Rocky Mountains, the Andes, the Himalayas, the Zagros Mountains in Iran, the Hijaz Mountains in Saudi Arabia and the highlands in Ethiopia. Over these high-elevation areas there are hardly any BC or DU sources; thus these values might be a product of retrieval errors related to surface elevation.

$\text{AAOD}_{550}$  in  $\text{CTL}_{\text{ECHAM}}$  is mostly underestimated globally. A pronounced underestimation is evident over tropical Africa, which relates to the low BC emissions of the emission inventory that we use, GFAS (v1.0). Typically, the biomass burning emissions of GFAS for black and organic carbon are multiplied by a scaling factor of 3.4 to obtain a similar AOD to that observed by MODIS (Kaiser et al., 2012; Veira et al., 2015). Here this scaling factor is not applied in order to let our data assimilation system estimate new scaling factors based on POLDER observations, distinctively for OC and BC emissions.  $\text{DAS}_{\text{ECHAM}}$  has considerably smaller differences than POLDER globally and especially over the tropics. The global MAE for  $\text{AAOD}_{550}$  is reduced from 0.0106 in  $\text{CTL}_{\text{ECHAM}}$  to 0.0077 in  $\text{DAS}_{\text{ECHAM}}$ .

The experiments are also evaluated with independent observations that are not assimilated. The scatterplots in Fig. 2 depict the evaluation of POLDER as well as the POLDER-collocated  $\text{CTL}_{\text{ECHAM}}$  and  $\text{DAS}_{\text{ECHAM}}$  against AERONET. All AERONET sites were collocated with the closest grid cell in one  $1 \times 1$  resolution on a 3-hourly basis. Cases where multiple stations belonged to the same grid cell and had observations at the same time were averaged. A similar evaluation analysis against AERONET for model data that are not collocated to POLDER is provided in Fig. S4 for  $\text{CTL}_{\text{ECHAM}}$  and  $\text{DAS}_{\text{ECHAM}}$ . In addition Figs. 3 and 4 depict an evaluation of these two experiments for selected AERONET stations representative of SS and BC, respectively.

The ME and MAE improve in  $\text{DAS}_{\text{ECHAM}}$  experiments compared with  $\text{CTL}_{\text{ECHAM}}$  for all variables, except the  $\text{AE}_{550-865}$  ME. The satellite  $\text{AE}_{550-865}$  is overestimated compared with AERONET by 0.096, which can partially contribute to the increase in the  $\text{AE}_{550-865}$  ME in  $\text{DAS}_{\text{ECHAM}}$ . Further, the unchanged high  $\text{AE}_{550-865}$  in the model is observed over land (Fig. 2f) where the observational uncertainty in POLDER  $\text{AE}_{550-865}$  is high (greater than 0.45) for most  $\text{AOD}_{550}$  bins (Fig. A1).

The uncertainty in POLDER observations is based on an evaluation with AERONET (see Appendix A). POLDER  $\text{AE}_{550-865}$  errors spread against AERONET (Fig. 2d) are similar to the  $\text{CTL}_{\text{ECHAM}}$  errors spread against AERONET (Fig. 2e). Notably the POLDER  $\text{AAOD}_{550}$  errors spread

against AERONET (Fig. 2g) are even greater than the  $\text{CTL}_{\text{ECHAM}}$  errors spread against AERONET (Fig. 2h). Despite this, there is a small improvement in MAE for both observables and a clear improvement in  $\text{AAOD}_{550}$  bias where the ME goes from  $-0.009$  in  $\text{CTL}_{\text{ECHAM}}$  to  $-0.004$  in  $\text{DAS}_{\text{ECHAM}}$ .

The improvement in  $\text{AE}_{550-865}$  and  $\text{AAOD}_{550}$  compared with AERONET after data assimilation is much clearer if we focus on AERONET stations in regions where the difference between  $\text{CTL}_{\text{ECHAM}}$  and  $\text{DAS}_{\text{ECHAM}}$  is large. This is mostly in regions with strongly modified SS and BC emissions, respectively. To investigate this improvement, an evaluation for selected stations is depicted in Figs. 3 and 4. In Fig. 3 four stations that are located in isolated islands over the ocean were selected in order to capture the changes in  $\text{AE}_{550-865}$  due to the adjusted SS emissions. In all cases  $\text{CTL}_{\text{ECHAM}}$  overestimates  $\text{AE}_{550-865}$ . After the adjusted emissions  $\text{AE}_{550-865}$  is improved with a reduction in ME of about 0.1 or higher (except in Midway Island). In Fig. 4, four regions with biomass burning and anthropogenic BC emissions were selected to study the changes in  $\text{AAOD}_{550}$ . In all cases the underestimation of  $\text{AAOD}_{550}$  in  $\text{CTL}_{\text{ECHAM}}$  improves after the adjusted emissions, especially in the sites over the biomass burning regions (Sahel stations and Mongu station), but also in regions with anthropogenic sources of BC (Europe and India). A similar improvement is observed for  $\text{SSA}_{550}$  over the same regions (Fig. S5).

From previous work (Tsikerdekis et al., 2021), we know that assimilating  $\text{AOD}_{550}$  along with  $\text{AE}_{550-865}$  and  $\text{SSA}_{550}$  results in a considerable  $\text{AOD}_{550}$  improvement, with a small improvement in size and absorption. Assimilating only  $\text{AOD}_{550}$  results in a considerable  $\text{AOD}_{550}$  improvement, with a small improvement in aerosol size, while having a very negative effect on the aerosol absorption. Our findings here confirm the importance of assimilating information on size and absorption in addition to AOD. It is important to note that future polarimeter instruments such as SPEXone and 3MI are expected to yield better retrievals (Hasekamp et al., 2019) and hence have the potential to estimate aerosol emissions better (Tsikerdekis et al., 2022a).

In addition, we evaluate the effect of the assimilation against MODIS Collection 5 Dark Target (Sayer et al., 2014) at  $1^\circ \times 1^\circ$  resolution. Specifically, we use a specialized version of MODIS designed for assimilation, which was corrected based on 4 years of AERONET observations (Hyer et al., 2011; Shi et al., 2011; Zhang and Reid, 2006). Figure 5 depicts the MODIS  $\text{AOD}_{550}$  for the year 2006 along with the differences in  $\text{CTL}_{\text{ECHAM}}$  and  $\text{DAS}_{\text{ECHAM}}$  from MODIS. Before the assimilation the model biases against MODIS follow a similar pattern to the biases observed against POLDER, with an underestimation of  $\text{AOD}_{550}$  over land (notably over biomass burning regions and Sahel) and an overestimation over the ocean. After the assimilation the negative bias over land is corrected, but the overestimation over the ocean remains. The ME and MAE improve from



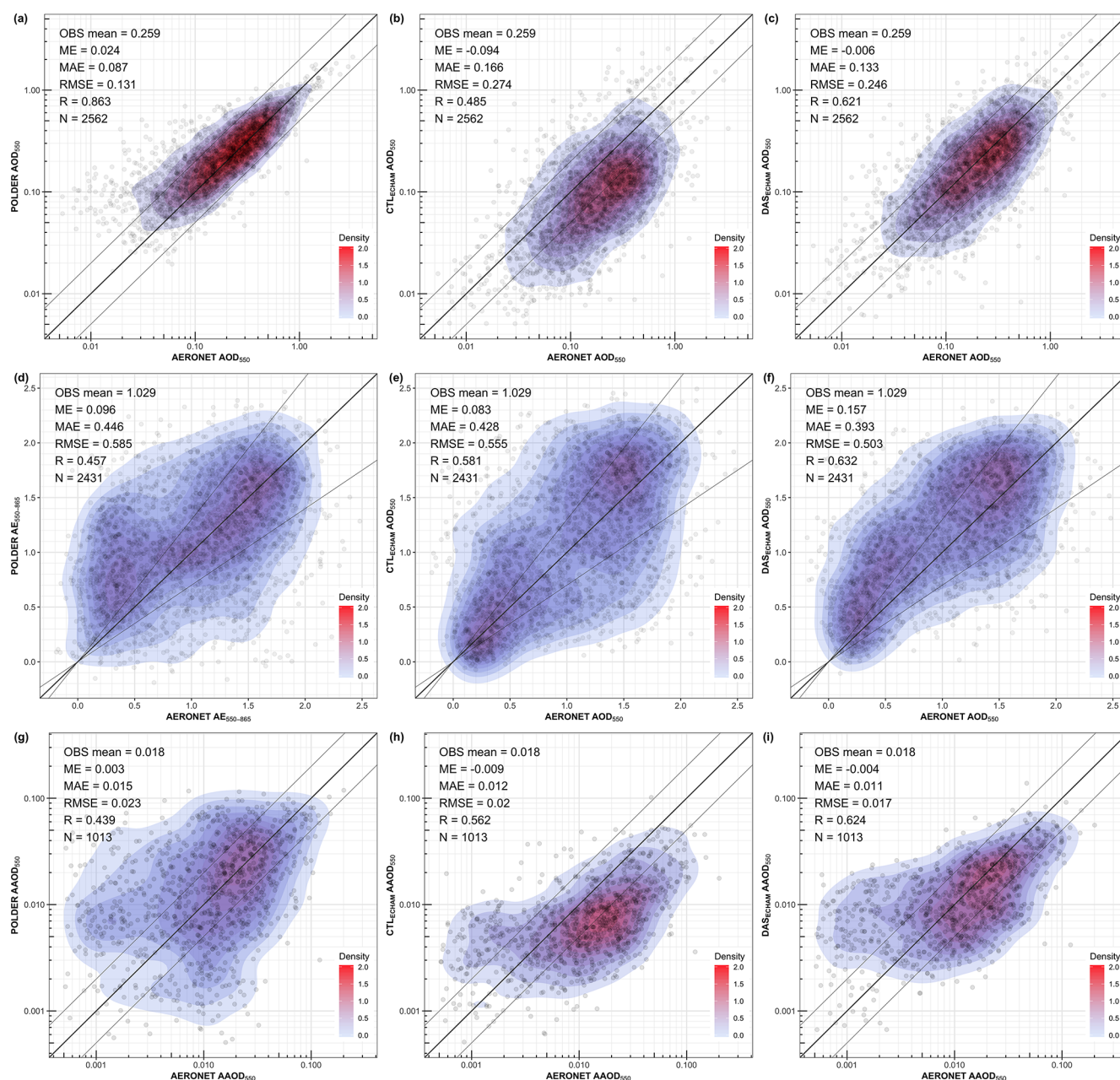


**Figure 2.** An evaluation of POLDER (first column), CTLECHAM (second column) and DASECHAM (third column) based on AERONET for the year 2006. The first, second and third rows correspond to the variables AOD<sub>550</sub>, AE<sub>550–865</sub> and AAOD<sub>550</sub>, respectively. The OBS mean refers to AERONET in all plots. The mean error (ME), mean absolute error (MAE), root mean square error (RMSE), Pearson correlation ( $R$ ) and the number of data points used in each case ( $N$ ) are depicted in the top left of each subplot. The AOD<sub>550</sub> and AE<sub>550–865</sub> evaluation is based on the AERONET version 3 level 2.0 direct sun algorithm, while the AAOD<sub>550</sub> evaluation is based on the AERONET version 3 level 1.5 direct sun and inversion algorithm.

−0.032 and 0.061 in the CTLECHAM experiment to 0.015 and 0.050 in the DASECHAM experiment. Further, we conduct a similar analysis to Fig. 2 but with the MODIS data. The scatterplots in Fig. 6 depict the collocated points between MODIS and AERONET for 2006, which are more than 5 times greater in number compared with POLDER. Similarly,

before the assimilation a negative bias is observed, which is corrected after the assimilation with a reduction in the spread of the errors as well. Specifically, the ME is reduced from −0.063 to 0.009 and the MAE from 0.132 to 0.118.

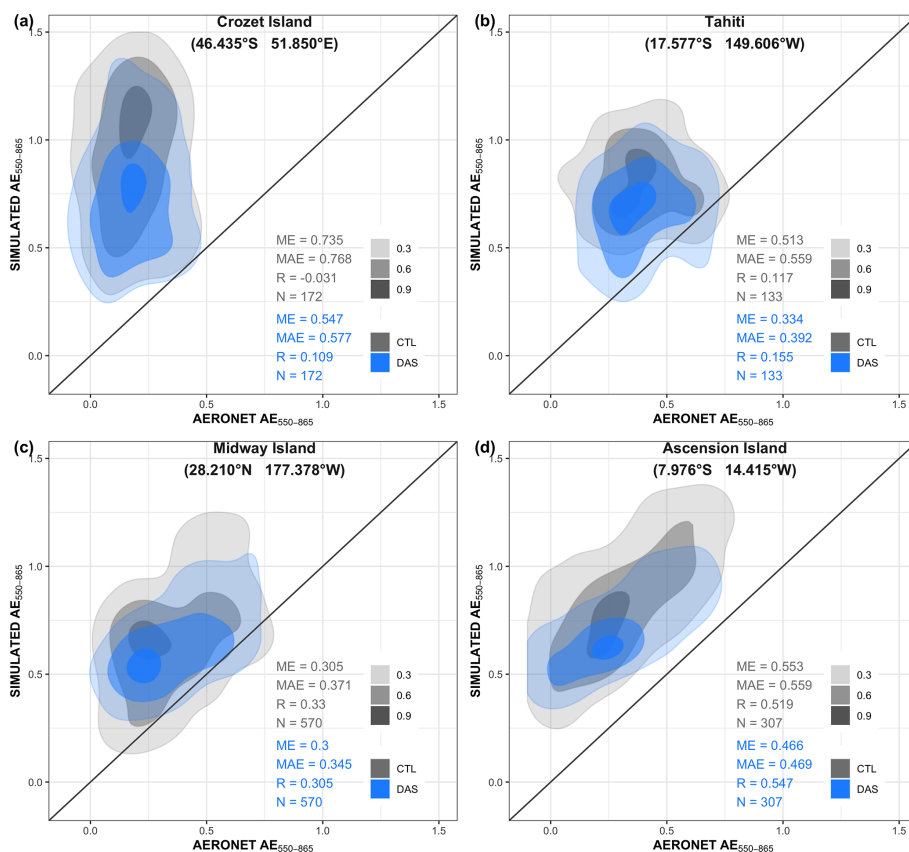


**Figure 3.** An  $AE_{550-865}$  evaluation of  $CTL_{ECHAM}$  and  $DAS_{ECHAM}$  based on selected AERONET stations (red points in Fig. 1d) for the year 2006. These stations are located in isolated islands over the ocean in order to capture the changes in  $AE_{550-865}$  due to SS emission changes. The shaded areas depict the 2D density estimate scaled to a maximum of 1 for 0.3, 0.6 and 0.9 intervals. The mean error (ME), mean absolute error (MAE), Pearson correlation ( $R$ ) and the number of data points used in each case ( $N$ ) are depicted for each subplot. The evaluation is based on the AERONET version 3 level 2.0 direct sun algorithm.

#### 4.2 Aerosol emission estimation from POLDER

The yearly emissions for several aerosol species are shown in Fig. 7. Dust and sea salt particles in the coarse mode dominate the total mass of aerosols, followed by sulfates and sea salt in the accumulation mode and organic carbon emissions. Note that sulfate total deposition is used as a proxy for sulfate formation in the atmosphere.  $SO_2$  emissions are primarily concentrated over the Northern Hemisphere, mainly over North America, Europe, India and Southeast Asia. The black carbon total mass is very low globally (although it is very important for aerosol absorption; see Fig. S3) and is concentrated over biomass burning regions and densely populated areas where high anthropogenic emissions occur.

The relative changes in yearly aerosol emissions because of the assimilated POLDER observations are depicted in Fig. 8. Grid cells with emissions lower than the global median value in each species are masked out (grey) in order to emphasize areas where aerosol emissions are not too low. Overall, emissions increase for all species (except in the sea salt accumulation mode), which coincides with the large un-

derestimation of both  $AOD_{550}$  and  $AAOD_{550}$  by  $CTL_{ECHAM}$  compared with POLDER (see Sect. 4.1).

Dust accumulation and coarse-mode emissions increase everywhere, except over Iran and the Gobi Desert during the coarse mode. Sea salt accumulation mode emissions are reduced almost everywhere in the world, while sea salt coarse-mode emissions increase. This illustrates the importance of assimilating the  $AE_{550-865}$  observations, since these changes reduce the  $AE_{550-865}$  overestimation compared with POLDER over the ocean. Organic carbon emissions increase everywhere globally and approximately by a factor of 3 in tropical Africa, 2.5 in the Amazon Basin and Indonesia, and 2 in Southeast Asia. Black carbon emissions increase approximately by a factor of 3 in the United States and 1.5 in tropical Africa and are slightly reduced in Southeast Asia and in parts of the Amazon Basin. In all cases the underestimated  $AAOD_{550}$  of  $CTL_{ECHAM}$  improves in  $DAS_{ECHAM}$ . Note that POLDER  $AAOD_{550}$  is overestimated over several high-altitude areas (as discussed in Sect. 4.1); thus emissions near these areas may have been inflated, since the correlation length of black carbon emissions perturbations in our data

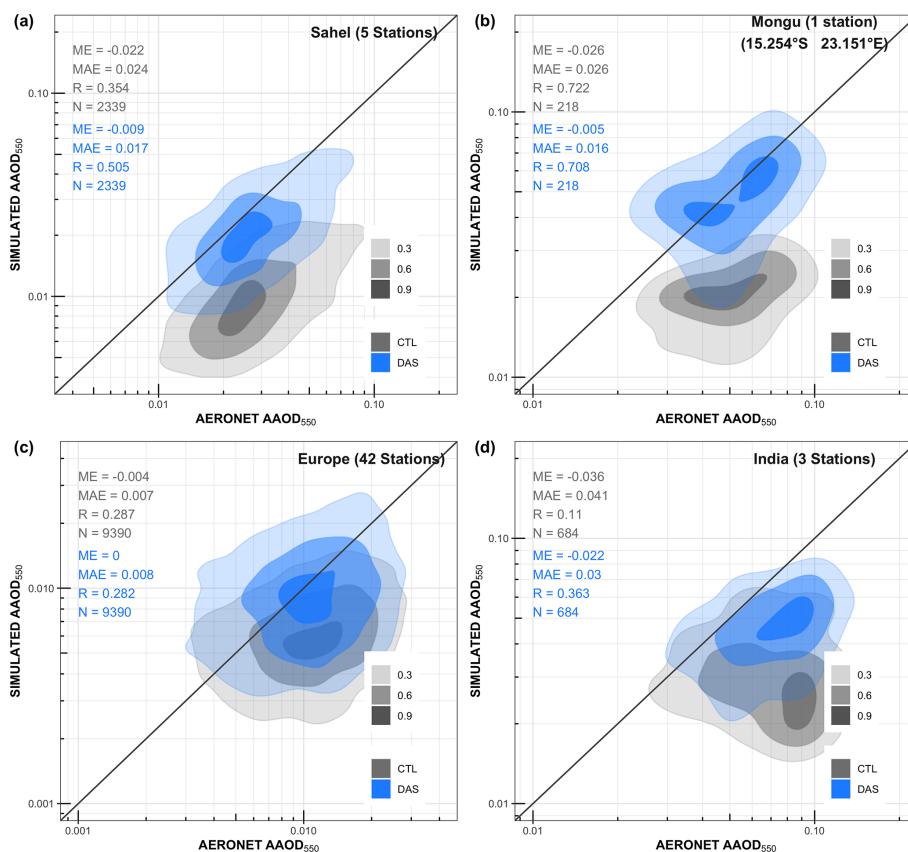


**Figure 4.** An  $\text{AAOD}_{550}$  evaluation of  $\text{CTL}_{\text{ECHAM}}$  and  $\text{DAS}_{\text{ECHAM}}$  based on selected AERONET sites (cyan points in Fig. 1g) for the year 2006. These stations are selected over regions where natural and anthropogenic emissions of BC occur. The shaded areas depict the 2D density estimate scaled to a maximum of 1 for 0.3, 0.6 and 0.9 intervals. The mean error (ME), mean absolute error (MAE), Pearson correlation ( $R$ ) and the number of data points used in each case ( $N$ ) are depicted for each subplot. The evaluation is based on the AERONET version 3 level 1.5 direct sun and inversion algorithm.

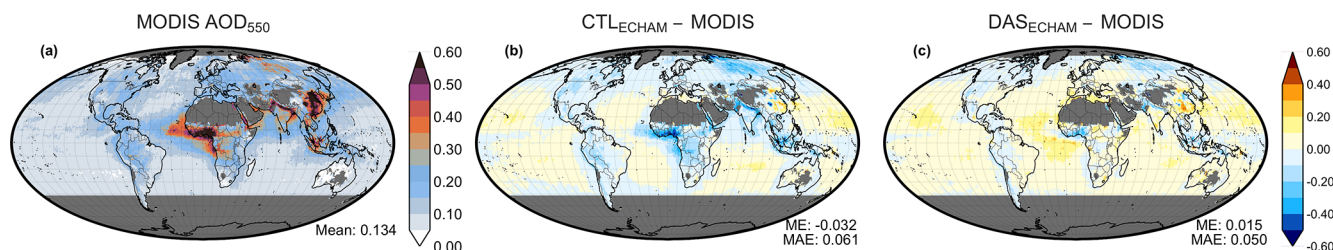


**Figure 5.** An evaluation of the  $\text{CTL}_{\text{ECHAM}}$  and  $\text{DAS}_{\text{ECHAM}}$  experiments, based on MODIS for the year 2006. The first column depicts MODIS  $\text{AOD}_{550}$ , while the second and third columns display the differences between  $\text{CTL}_{\text{ECHAM}} - \text{POLDER}$  and  $\text{DAS}_{\text{ECHAM}} - \text{POLDER}$ , respectively. The global mean, global mean error (ME) and global mean absolute error (MAE) are depicted in the bottom-right corner of each plot.

assimilation system is fairly big ( $25^\circ$ ). The  $\text{SO}_2$  emissions increase in Europe as well as in North America by about a factor of 1.5 and remain almost the same over Southeast Asia. The same changes are observed for the  $\text{SO}_4$  total deposition.

Considering the relatively big changes in emissions, ranging from 1.5 to 3.0 for large portions of the globe, and the

small improvements when evaluating the observables with all AERONET stations, it can be concluded that the network spatial coverage may not be sufficient to capture the global aerosol changes. This may be more relevant for  $\text{AE}_{550-865}$  and  $\text{AAOD}_{550}$  than for  $\text{AOD}_{550}$ , where it is clearly improved (Fig. 2). Note that  $\text{AE}_{550-865}$  and  $\text{AAOD}_{550}$  also improve

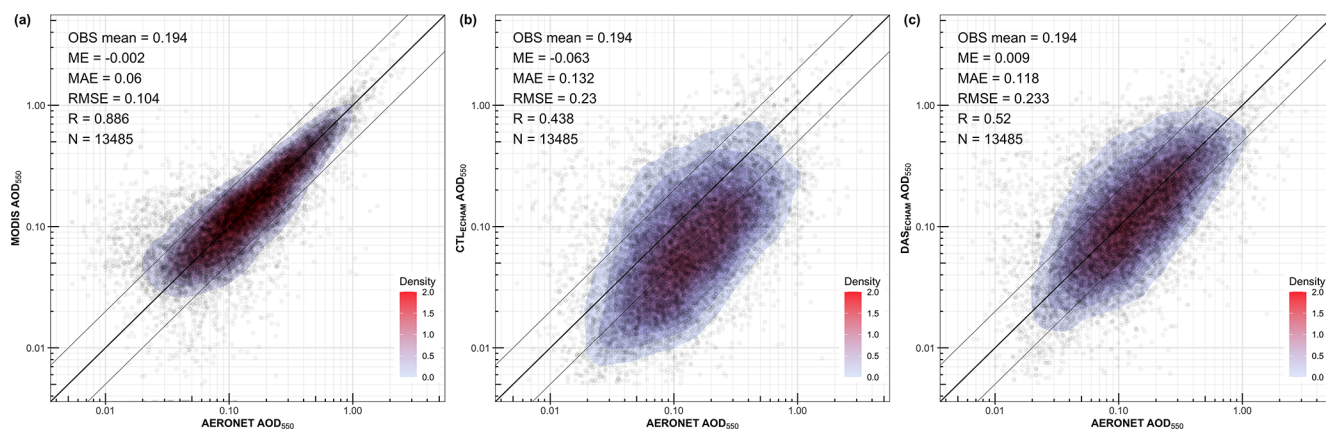


**Figure 6.** An AOD<sub>550</sub> evaluation of MODIS (first column), CTL<sub>ECHAM</sub> (second column) and DAS<sub>ECHAM</sub> (third column) based on AERONET for the year 2006. The OBS mean refers to AERONET in all subplots. The mean error (ME), mean absolute error (MAE), root mean square error (RMSE), Pearson correlation ( $R$ ) and the number of data points used in each case ( $N$ ) is depicted in the top left of each subplot. The AOD<sub>550</sub> evaluation is based on AERONET Version 3 Direct Sun Algorithm Level 2.0.

against AERONET when we focus on specific areas (Figs. 3 and 4).

#### 4.3 Global aerosol emissions and comparison with other studies

In this subsection the new global-scale estimated emissions are presented and compared with previous studies. Some of these studies contain an ensemble of simulations (e.g., CMIP5, AEROCOM phase I and III), while others may include emissions based on data assimilation experiments. Note that the annual mean emissions for some studies may be regional and not global estimates (e.g., Chen et al., 2019; Escribano et al., 2017) and also may not refer to the year 2006, which is the reference year for our study. These issues, which are independent from inter-model differences in physics (e.g., emission schemes), chemistry parameterizations and prescribed emission inventories, may enhance the emissions differences from study to study. Thus, the comparison of our estimated emissions with the emissions from other studies is expected to differ and serves more as a qualitative comparison. The studies with an ensemble of models are presented in terms of the ensemble median, ensemble standard deviation and relative diversity, which is equal to the ratio of the standard deviation to the median and is then multiplied by 100.

##### 4.3.1 Dust emissions

Dust (DU) and sea salt (SS) global emissions are shown in Fig. 9. The emissions of these species are highly dependent on the simulated aerosol size range of each model; the wind distribution in each model; and the activation areas, where dust can be emitted. Hence the emissions differ a lot from model to model (Wu et al., 2020). Previous studies have also indicated that emissions fluxes for DU and SS are also highly

resolution dependent (Guelle et al., 2001; Laurent et al., 2008). Specifically, ECHAM–HAM showed that DU emissions may differ by a factor of more than 2 globally, with local changes in emissions being even higher between a simulation at T63 (CTL<sub>ECHAM</sub>) to T31 (RES<sub>LOW</sub>) horizontal resolution, while smaller local differences were observed in SS emissions (Fig. S6). It is important to note here that the emissions estimation for a lower-resolution (T31) data assimilation experiment (not shown) was very close ( $\sim 1500 \text{ Tg yr}^{-1}$ ) to the estimated emissions by the higher resolution (T63).

The global dust emissions of CTL<sub>ECHAM</sub> are  $1105 \text{ Tg yr}^{-1}$  and are increased to  $1419 \text{ Tg yr}^{-1}$ , a percentage change equal to 28%. These changes bring emissions closer to the estimates of many other studies, as indicated with the different colored points in Fig. 9. The ensemble median of AEROCOM I (including 14 models) is  $1572 \text{ Tg yr}^{-1}$ , which lies quite close to the estimates of this study.

As with the AEROCOM I models, AEROCOM III tends to underestimate AOD and overestimate AE over the Sahara and Middle East according to AERONET, which suggests that the coarse aerosol emissions are underestimated relative to the fine-mode emissions (Gliß et al., 2021). The same can be seen in the CTL<sub>ECHAM</sub> and DAS<sub>ECHAM</sub> simulations (Fig. S7), with a mean error in AE<sub>550–865</sub> of 0.055 and 0.146, respectively, against AERONET. Note that POLDER AE<sub>550–865</sub> over the Sahara is biased high based on AERONET; thus these observations were not assimilated (see Appendix A). The overestimated AE<sub>550–865</sub> suggests that the estimated dust emissions in DAS<sub>ECHAM</sub> should probably be higher, since the emissions of dust in the coarse mode, which correspond to 98% of the total emitted dust globally, need to be higher.

The DU emissions ensemble median of CMIP5 models (15 models) is  $2716 \text{ Tg yr}^{-1}$ , with a  $2177 \text{ Tg yr}^{-1}$  standard deviation and 80% diversity (Wu et al., 2020). Some of the

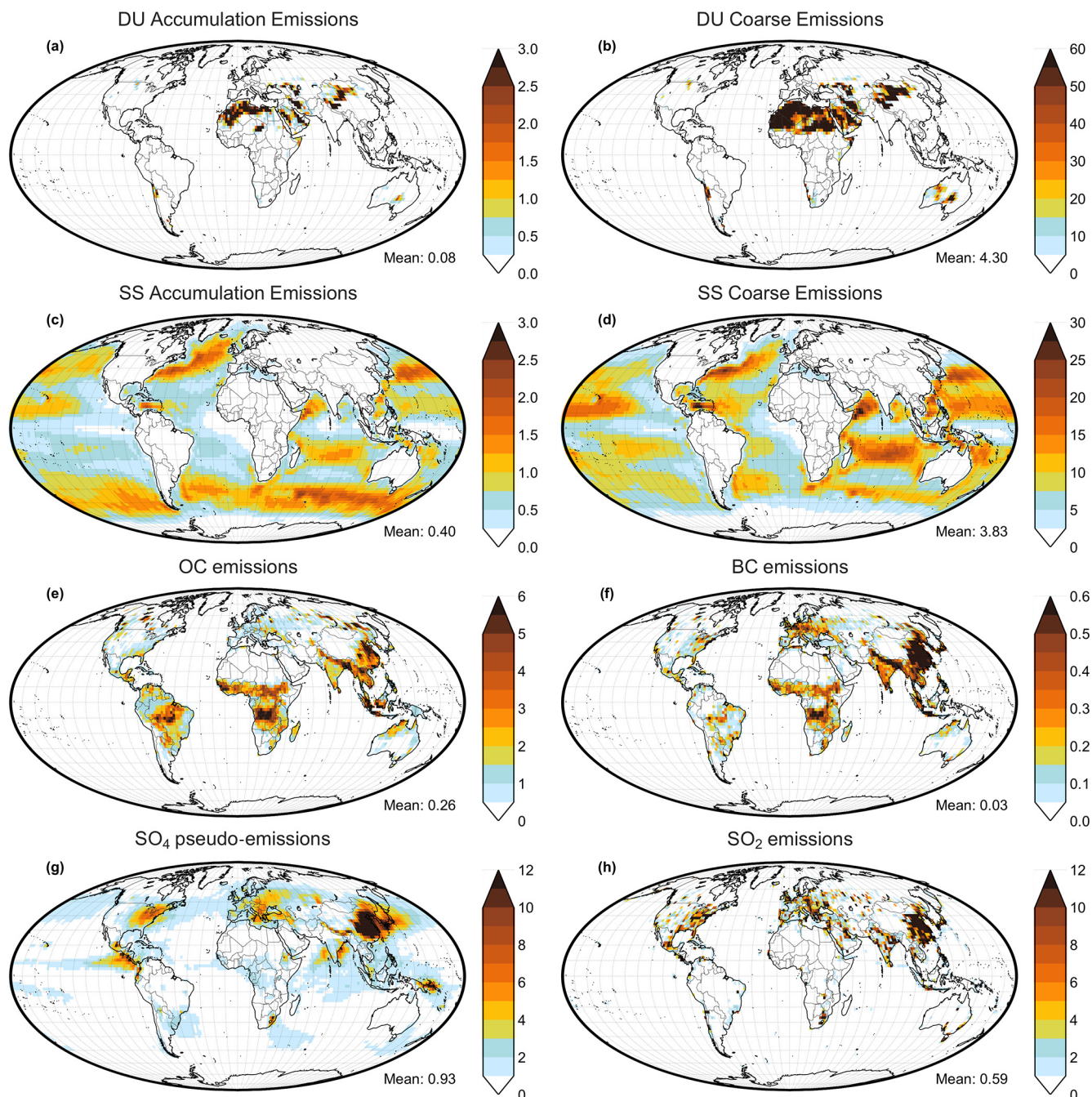


**Figure 7.** Aerosol emissions (kg km<sup>-2</sup> d<sup>-1</sup>) of the CTL<sub>ECHAM</sub> experiment for 2006. The global mean is depicted in the bottom-right corner of each map. The pseudo-emissions of SO<sub>4</sub> are based on the SO<sub>4</sub> total deposition.

factors that contribute to this diversity are the difference in the simulated size range (e.g., from 0.06 to 63 μm for some models and < 16 μm for others), the global percentage where dust can be emitted that ranges from 2.9 % to 18 % and the differences in the spatial distribution of dust emissions.

The amount of the estimated dust emission due to data assimilation or observationally constrained methods in previous studies (Chen et al., 2018, 2019, 2022; Escribano et al.,

2017; Huneeus et al., 2012; Schutgens et al., 2012) differs considerably both before and after observationally constraining the dust emissions for reasons that have already been discussed. In all these studies dust emissions change between 27 % and 62 % with a median value of 46 %. The percentage change of dust emissions due to the assimilated POLDER observations in the present study is 28 %, which lies in the

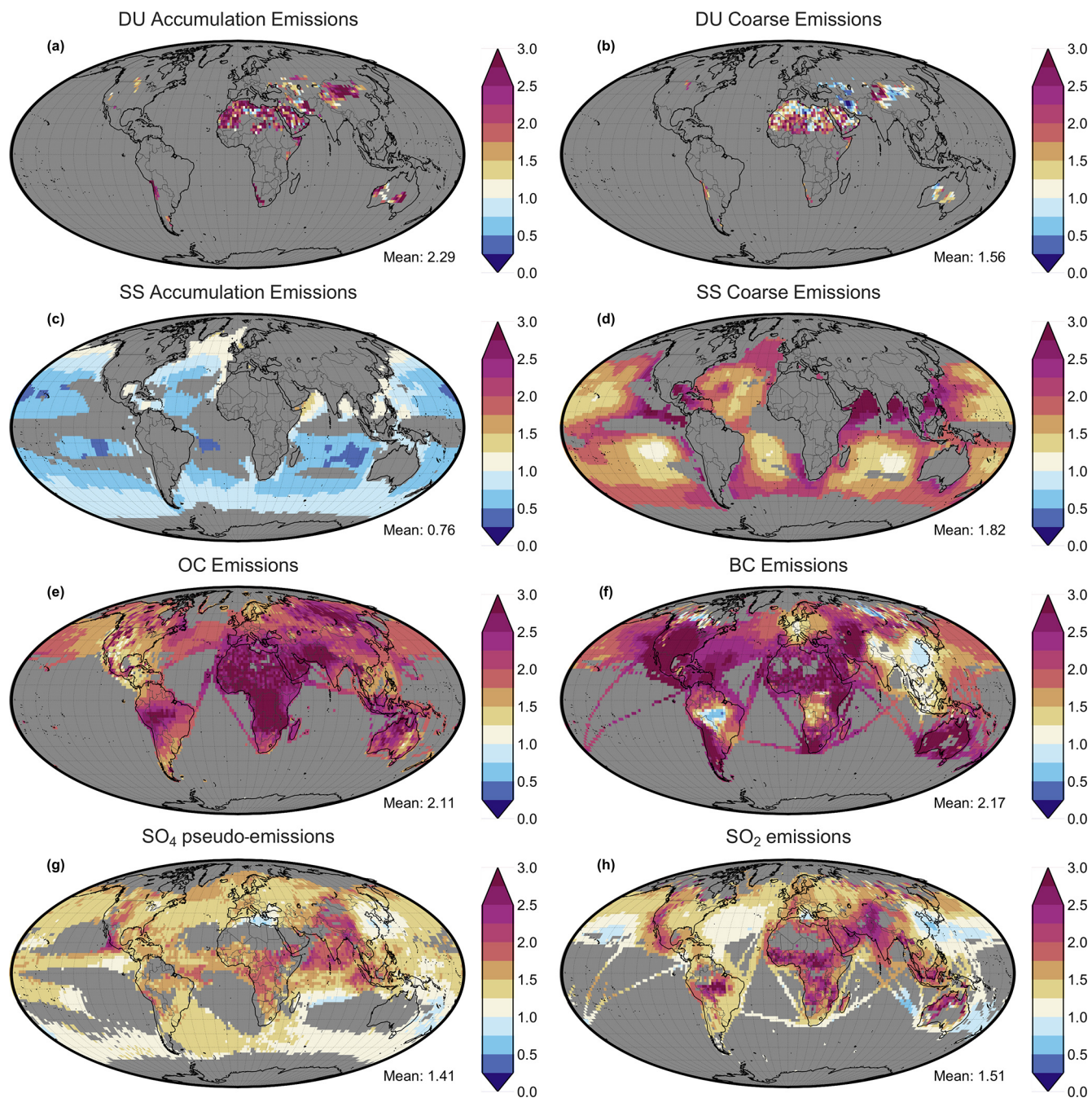


**Figure 8.** Relative changes in aerosol emissions due to the assimilated POLDER observations ( $DAS_{ECHAM}$  divided by  $CTL_{ECHAM}$ ) for 2006. The global mean is depicted in the bottom-right corner of each map. Grey grid cells contain emissions lower than the global median value of each species and are excluded from these maps.

lower end of the percentage change range of previous studies.

A recent study where dust emissions were constrained in terms of mass extinction efficiency, dust size distribution and dust optical depth has revealed the importance of including the very coarse particles (up to  $20\ \mu\text{m}$  in geometric diameter) for the total emitted dust mass in GCMs (Kok et al., 2021).

According to the constrained experiment,  $1800\ \text{Tgyr}^{-1}$  (with a  $1\sigma$  uncertainty between  $1200$  and  $2700\ \text{Tgyr}^{-1}$ ) was reported for emissions of up to  $10\ \mu\text{m}$ , which is close to our estimate and the ensembles of other studies. In contrast, for emissions of up to  $20\ \mu\text{m}$ ,  $4700\ \text{Tgyr}^{-1}$  (with a  $1\sigma$  uncertainty between  $3300$  and  $9000\ \text{Tgyr}^{-1}$ ) was reported. The contribution of emitted particles between  $10$  and  $20\ \mu\text{m}$  to

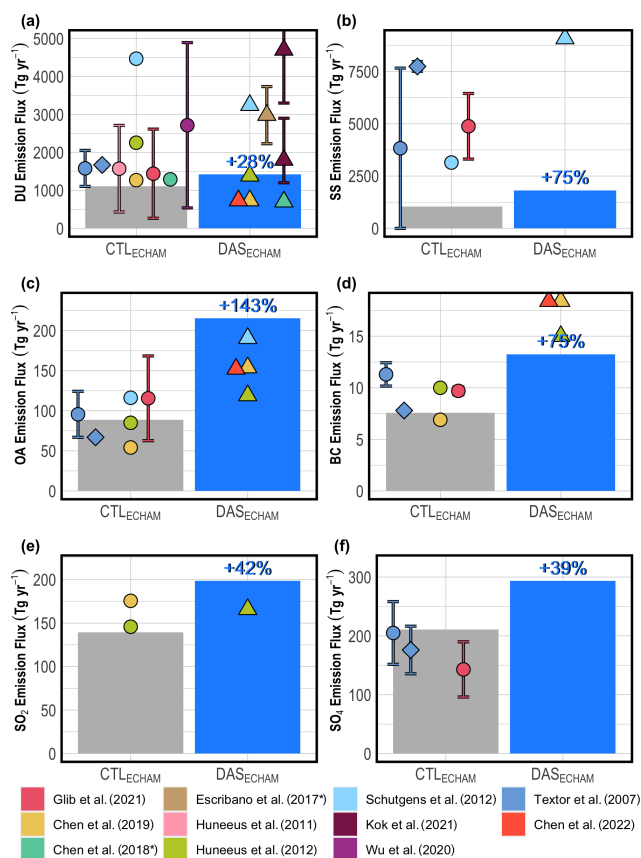


**Figure 9.** Global aerosol emissions in 2006 for dust (DU), sea salt (SS), organic aerosol (OA), black carbon (BC) and sulfur dioxide ( $\text{SO}_2$ ) and the total deposition of sulfates ( $\text{SO}_4$ ) ( $\text{Tg yr}^{-1}$ ). The percentage change of the estimated emissions over  $\text{DAS}_{\text{ECHAM}}$  is estimated based on the emissions of  $\text{CTL}_{\text{ECHAM}}$ . The circles depict the reported emissions from other studies. The diamonds depict the sensitivity study in Textor et al. (2007), which is explained in the text. The triangles illustrate the emissions estimated from past data assimilation studies. OA is estimated by multiplying the emissions of OC by 1.4 for the experiments of this study, as well for the reported emissions in Schutgens et al. (2012) and Chen et al. (2019, 2022). The  $\text{SO}_4$  total deposition is used as a proxy for  $\text{SO}_4$  pseudo-emissions.  $\text{SO}_2$  emissions for Chen et al. (2019) and Huneus et al. (2012) were reported in  $\text{Tg S yr}^{-1}$ ; thus they were multiplied by 2 in order to be converted into  $\text{Tg SO}_2 \text{ yr}^{-1}$ . The asterisk symbol in some studies indicate that the reported emissions are regional and not global. The yearly emissions from Schutgens et al. (2012) are an extrapolation of a single month's (January) experiment. The two Kok et al. (2021) estimates refer to emissions for DU particles of up to  $10 \mu\text{m}$  (low estimate) and up to  $20 \mu\text{m}$  (high estimate) in geometric diameters (see text for more details).

the total dust emissions was close to 65 %, but the contribution to the total  $\text{AOD}_{550}$  in the same size range was about 7 %. Based on these results, the inclusion of a super-coarse insoluble mode in ECHAM–HAM will increase total emissions and  $\text{AOD}_{550}$  over dust areas as well as the estimated emissions by our data assimilation system. The inclusion of

coarse dust particles ( $> 10 \mu\text{m}$ ) in GCMs is crucial for the total mass of dust emissions, absorption (Kok et al., 2021) and the nutrient contribution of dust to land and ocean ecosystems (Kim et al., 2014), but in terms of dust scattering the effect would be quite limited since their mass extinction efficiency relative to smaller particles is considerably smaller (particularly for the shortwave radiation).

#### 4.3.2 Sea salt emissions

The SS emissions for the  $\text{CTL}_{\text{ECHAM}}$  experiment is  $1039 \text{ Tg yr}^{-1}$ , which in comparison with the other studies is considerably lower. The coarse mode, which contains 90 % of the total emission mass of SS, is probably underestimated in the sea salt scheme that was used for our experiments (Long et al., 2011). This is also supported from an evaluation with POLDER, where the  $\text{CTL}_{\text{ECHAM}}$  experiment overestimated  $\text{AE}_{550-865}$  over the ocean (Fig. 1e). The ensemble median of AEROCOM III is  $4880 \text{ Tg yr}^{-1}$  (excluding ECMWF-IFS), with a standard deviation of  $1568 \text{ Tg yr}^{-1}$  and a diversity of 32 % (Gliß et al., 2021). ECMWF-IFS with an estimate of  $50\,000 \text{ Tg yr}^{-1}$  was not included since the emission scheme (Grythe et al., 2014) produces SS particles that are too large and that have very short lifetimes (Gliß et al., 2021). Note that the AEROCOM III ensemble median tends to underestimate the AE by 22 %, mainly over the ocean, according to AATSR-SU observations, thus overestimating the SS particle size and to an extent the mass flux of emissions (Gliß et al., 2021). Based on a fraction of AEROCOM I models, Textor et al. (2007) estimated an ensemble median of  $3830 \text{ Tg yr}^{-1}$  with a standard deviation of  $3830 \text{ Tg yr}^{-1}$  that results in a diversity of 100 %.

The assimilation of POLDER observations increases the global emissions to  $1850 \text{ Tg yr}^{-1}$  in  $\text{DAS}_{\text{ECHAM}}$ , which corresponds to a percentage change of +82 % with respect to the  $\text{CTL}_{\text{ECHAM}}$  experiment. Although SS emissions are still low (compared with the majority of AEROCOM III models, for example), ECHAM–HAM can reproduce the AOD adequately both before and after the assimilation (Fig. 1b and c), indicating that the mass extinction coefficient (MEC) of the model is high. A high MEC is related to more fine SS particles, as indicated by the evaluation against POLDER  $\text{AE}_{550-865}$  (Fig. 1). Further, a high MEC could partially be explained by the overestimated RH that enhances water uptake into SS and increases AOD. This topic is discussed further in Sect. 4.4. So far only one data assimilation study has provided an aerosol emission estimate. Schutgens et al. (2012) found that the SS emissions increased after assimilating AERONET stations and MODIS-Aqua AOD over the ocean. It is noteworthy that their yearly emissions were estimated from a monthly (January 2009) experiment.

### 4.3.3 Organic aerosol emissions

In order to compare our emissions with other studies, OC emissions were converted to organic aerosol (OA) by multiplying them by a factor of 1.4 (Tegen et al., 2019). The OA global emission from the CTL<sub>ECHAM</sub> run is equal to 88.6 Tg yr<sup>-1</sup>. The AEROCOM III ensemble median is 116 Tg yr<sup>-1</sup>, with a large standard deviation (53 Tg yr<sup>-1</sup>) and diversity (46 %). Inter-model differences between the AEROCOM III models are associated with differences in initial primary organic aerosol emissions, differences in secondary organic aerosol formation and differences in the conversion of OC from diverse sources of OA (Gliß et al., 2021). For example, the conversion factors used to convert OC to OA can range between 1.4 and 2.6. These values are used by many AEROCOM III models that multiply all OC emissions, independently of the source type. But there are also models (e.g., NorESM2) that use different conversion factors depending on the source type, for example, 1.6 for fossil fuel sources and 2.6 for biomass burning sources (Gliß et al., 2021).

The assimilated POLDER observations increase the OA emissions to 215.2 Tg yr<sup>-1</sup> (+143 %) in DAS<sub>ECHAM</sub>, which is higher than in any other emission estimation study. All previous data assimilation studies have indicated an increase in OA emissions when observations are considered. The amount of increase differs from study to study, but the increasing signal is apparent in all, independently of the observations that were assimilated in each case. The emissions in Schutgens et al. (2012), Chen et al. (2019) and Chen et al. (2022) are reported in OC; thus they were multiplied by 1.4 to get an approximation of the OA emissions. The OA emissions increase in Schutgens et al. (2012) from 116.2 to 190.4 Tg yr<sup>-1</sup> (+64 %), in Huneus et al. (2012) from 85 to 119 Tg yr<sup>-1</sup> (+40 %) and in Chen et al. (2019) from 54.2 to 153.9 Tg yr<sup>-1</sup> (+184 %). Note that the increase in organic aerosol emissions in DAS<sub>ECHAM</sub> is significantly stronger for natural biomass burning sources (+193 %) than for anthropogenic sources (+115 %).

### 4.3.4 Black carbon emissions

The black carbon (BC) global emission is 7.6 Tg yr<sup>-1</sup> for the CTL<sub>ECHAM</sub> experiment. Since BC is highly absorbing, the estimated emissions will highly depend on the assimilation of SSA (or AAOD). Aerosol absorption information can be obtained by POLDER, and, as shown previously, the assimilation of absorbing observations is essential in order to correctly estimate the BC mixing ratio and accurately simulate the absorption in a model (Tsikerdekis et al., 2021). The CTL<sub>ECHAM</sub> experiment underestimates AAOD<sub>550</sub> compared with POLDER; thus the BC emissions increase in DAS<sub>ECHAM</sub> to 13.3 Tg yr<sup>-1</sup> (+75 %). Previous data assimilation studies have shown a similar increasing tendency to OC emissions. Specifically, the BC emissions increase in

Huneus et al. (2012) from 10 to 15 Tg yr<sup>-1</sup> (+50 %) and in Chen et al. (2019) from 6.9 to 18.4 Tg yr<sup>-1</sup> (+166 %).

Note that the biomass burning emissions of organic and black carbon are based on GFAS emissions. The biomass burning emissions in DAS<sub>ECHAM</sub> increase by 193 % and 90 % (not shown) compared with CTL<sub>ECHAM</sub>, which correspond to scaling factors equal to 2.93 and 1.90, respectively. These new scaling factors are distinctively estimated for organic and black carbon and are based on the assimilation of POLDER observations that includes absorption information; they can thus be used by future studies to scale the GFAS emissions. Past studies have proposed a scaling factor of 3.4 for GFAS emissions based on an AOD evaluation (Kaiser et al., 2012; Tegen et al., 2019; Veira et al., 2015), which was not applied in this study in order to estimate new scaling factors based on the assimilation of POLDER observations.

### 4.3.5 Sulfates and precursors emissions

The total deposition of SO<sub>4</sub>, which we use as a proxy for SO<sub>4</sub> pseudo-emissions, or rather the total chemical production of SO<sub>4</sub> in the atmosphere, along with the global emissions of SO<sub>2</sub>, are depicted in Fig. 9. The global pseudo-emission of SO<sub>4</sub> is 210.9 Tg yr<sup>-1</sup> for CTL<sub>ECHAM</sub>. The pseudo-emission of SO<sub>4</sub> for the AEROCOM III ensemble median for the year 2010 is 143 Tg yr<sup>-1</sup>, with a standard deviation of 46.9 Tg yr<sup>-1</sup> and a diversity of 33 % (Gliß et al., 2021). ECHAM–HAM and ECHAM–SALSA have among the highest SO<sub>4</sub> pseudo-emissions in this ensemble (218 and 216 Tg yr<sup>-1</sup>, respectively), which indicates that the production of SO<sub>4</sub> from SO<sub>2</sub> is possibly higher or SO<sub>2</sub> loss is possibly lower in these two models compared with the other AEROCOM III models. Further, Textor et al. (2007) noted that the differences in SO<sub>4</sub> production among AEROCOM I models remain almost the same, even when the same prescribed emissions of SO<sub>2</sub> are used, thus highlighting that inter-model differences in SO<sub>4</sub> may primarily be caused by differences in gain and loss processes rather than by differences in the primary SO<sub>2</sub> emissions. The production and loss processes of SO<sub>4</sub> are discussed in more detail in Sect. 4.4.2.

The SO<sub>2</sub> emission of CTL<sub>ECHAM</sub> is 139.6 Tg yr<sup>-1</sup>. The respective value for the CEDS emission inventory used by the CMIP6 models is 123.4 Tg yr<sup>-1</sup> (not shown in Fig. 9). The SO<sub>2</sub> emissions in the HTAP v2 emission inventory for 2010 used in Chen et al.'s (2019) study are higher (175.6 Tg yr<sup>-1</sup>) than CTL<sub>ECHAM</sub>, while SO<sub>2</sub> emissions in Huneus et al. (2012) for 2002 are closer (145.8 Tg yr<sup>-1</sup>) compared with CTL<sub>ECHAM</sub>. Only the later study has provided a new estimate for SO<sub>2</sub> emissions based on the assimilation of total and fine AOD of MODIS, which increased the SO<sub>2</sub> emissions to 165.8 Tg yr<sup>-1</sup> (+14 %). In DAS<sub>ECHAM</sub> the SO<sub>2</sub> emissions increase to 198.4 Tg yr<sup>-1</sup> (+42 %), which is higher than the reported emissions of Chen et al. (2019) and Huneus et al. (2012).



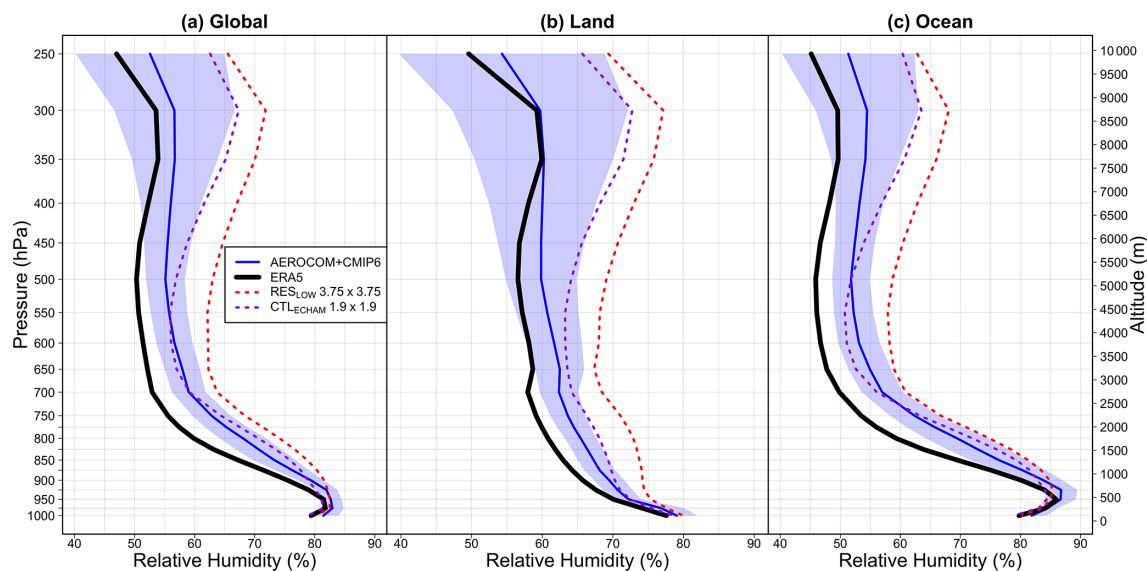


**Figure 10.** The relative humidity profile for a multi-model ensemble mean from 15 simulations that includes AEROCOM III and CMIP6 models (blue) along with ERA5 (black) for the year 2010. The shaded area represents the standard deviation of the ensemble. The CTL<sub>ECHAM</sub> and RES<sub>LOW</sub> experiments are also depicted.

#### 4.3.6 Overestimated relative humidity and the impact on aerosol optical properties

In this subsection we investigate the effect of errors in relative humidity and resulting errors in aerosol water uptake on the estimated emissions. In Fig. 10, we compare the mean and standard deviation of the relative humidity profiles of ECHAM, AEROCOM (eight models) and CMIP6 (seven models) with ERA5. ERA5 is set as the reference, and since it is a reanalysis product where numerous meteorological observations were assimilated and compared with all the other GCMs, the simulated RH should be closer to the truth. The majority of the models in this ensemble overestimates RH, both over land and over the ocean (Fig. 10c and b), except the AEROCOM III simulation conducted with the GFDL-AM4, GEOS and MIROC-SPRINTARS models, where the simulated profile of relative humidity is closer to ERA5, and their horizontal resolution is at least 2 times higher compared with the other simulations. None of the models underestimates the RH profile compared with ERA5. In addition to this ensemble, ECHAM–HAM simulations conducted for the year 2006 with different horizontal resolutions are also shown (CTL<sub>ECHAM</sub>, RES<sub>LOW</sub>). Clearly there is a dependence between the horizontal resolution of ECHAM–HAM and its capability to accurately simulate RH profiles. It is known that the current horizontal resolution of GCMs cannot directly resolve humidity’s small-scale spatial variability; thus it is parameterized (Lin, 2014). This is probably what is causing the differences in the RH profile compared with ERA5, but this is a topic that is out of the scope of our study. Note that the interannual ERA5 RH variability for the years

2006 (current study experiments) and 2010 (AEROCOM III) is minuscule (not shown).

The overestimation of RH for aerosol water uptake is the most critical for the lower troposphere ( $< \sim 3$  km or about 700 hPa), where RH is high enough ( $> 50\%$ ) for water uptake to be relevant (Fig. 11) and where most of the soluble aerosols exist. This overestimation is mostly concentrated over the ocean (Fig. S8), but there are also land areas where substantial overestimation of relative humidity is observed (e.g., East Asia). In order to quantify how aerosol properties are affected by the overestimation of the RH profile by ECHAM–HAM, an additional experiment (CTL<sub>ERA5</sub>) that used the RH profile of ERA5 to determine the growth factor in ECHAM–HAM was conducted. Note that this modification affects only aerosol optical properties (scattering and absorption) in ECHAM–HAM, while the water cycle (precipitation and evaporation) of the model remains unaltered.

Figure 11 depicts the mean aerosol extinction profile for the CTL<sub>ECHAM</sub> and CTL<sub>ERA5</sub> experiments. The aerosol extinction of insoluble particles is identical between the two experiments since they remain unaffected by aerosol water uptake changes. In contrast, the aerosol extinction of soluble particles in CTL<sub>ERA5</sub> exhibits considerably lower aerosol extinction compared with CTL<sub>ECHAM</sub>. Over land this difference reaches the maximum close to the surface and declines with height to up to 600 hPa ( $\sim 3800$  m) where it becomes zero. Over the ocean, the difference is small close to the surface, peaks at 825 hPa ( $\sim 1500$  m) and slowly declines to up to 650 hPa ( $\sim 3200$  m) where it becomes zero.

Note that over the ocean ECHAM–HAM strongly overestimates RH profiles consistently over most grid cells,

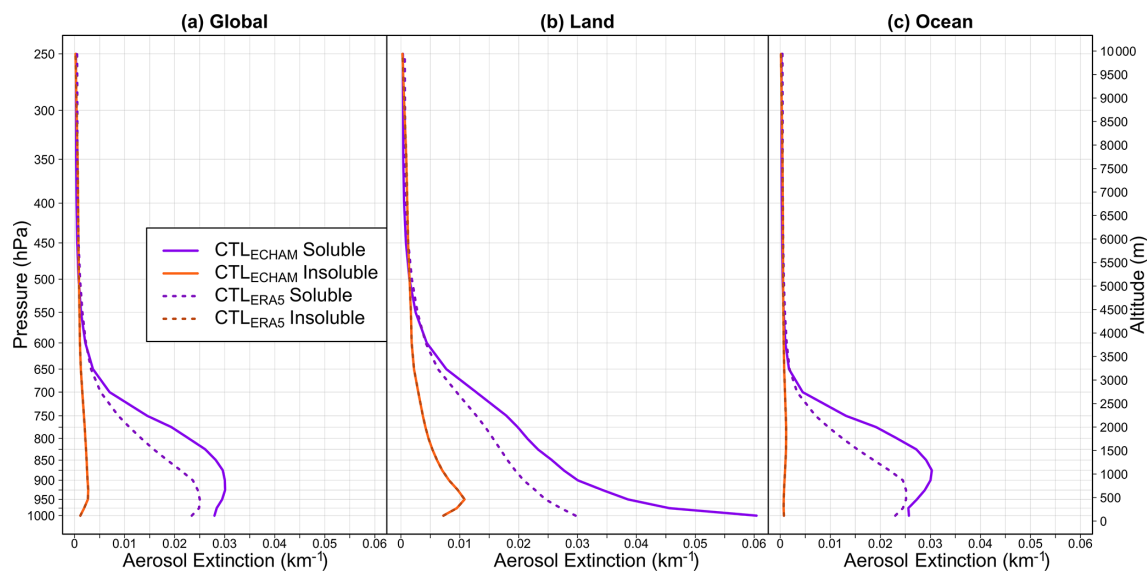


**Figure 11.** Aerosol extinction profiles ( $\text{km}^{-1}$ ) of  $\text{CTL}_{\text{ECHAM}}$  and  $\text{CTL}_{\text{ERA5}}$  for soluble and insoluble aerosols.

enhancing the growth of aerosols, which are mainly SS aerosols. In contrast, over land RH is overestimated in East Asia, Europe and the eastern part of North America, where soluble  $\text{SO}_4$  production is high, and underestimated over Sahel and the western part of the United States where insoluble DU particles are not affected by water uptake (Fig. S1). Consequently, over the ocean aerosol extinction profile differences (Fig. 11c) match the overestimation of RH by ECHAM–HAM (Fig. 10c), while over land this is not the case (Figs. 11b and 10b). Most interestingly, over high-density population areas (eastern China, Europe, North America), where high emissions of anthropogenic  $\text{SO}_2$  (precursor of  $\text{SO}_4$ ) occur, the aerosol extinction difference between  $\text{CTL}_{\text{ECHAM}}$  and  $\text{CTL}_{\text{ERA5}}$  is even greater, indicating that aerosol extinction of anthropogenic-induced aerosols is incorrectly inflated in ECHAM–HAM (and possibly in many other GCMs) because of the RH overestimation.

The global contribution of water condensed on the surface of aerosol particles (WAT) to total  $\text{AOD}_{550}$  changes from 62 % to 52 % from the  $\text{CTL}_{\text{ECHAM}}$  experiment to the  $\text{CTL}_{\text{ERA5}}$  experiment. For reference, the contribution of water  $\text{AOD}_{550}$  to total  $\text{AOD}_{550}$  in K. Zhang et al. (2012) was reported to be 70 % using ECHAM5–HAM2, which was nudged to ERA-40 for the year 2000. Although a 10 % decrease is significant, water aerosol optical depth remains the largest contributor of total  $\text{AOD}_{550}$  in  $\text{CTL}_{\text{ERA5}}$ , followed by DU (27 %),  $\text{SO}_4$  (11 %), OC (5 %), SS (5 %) and BC (1 %).

Changes in  $\text{AOD}_{550}$ ,  $\text{AE}_{550-865}$  and  $\text{AAOD}_{550}$  because of the overestimated RH are depicted in Fig. 12. Globally  $\text{AOD}_{550}$  is reduced by 0.015 (18 %);  $\text{AE}_{550-865}$  increases by 0.046; and  $\text{AAOD}_{550}$  is virtually unchanged, since BC and DU, which contribute 96 % of the global  $\text{AAOD}_{550}$  (Fig. S3), are insoluble. Regionally, the  $\text{AOD}_{550}$  change is by far the

strongest over East Asia, which can be explained by the presence of large loading of hydrophilic  $\text{SO}_4$  aerosol particles (Fig. S1e). The same holds, to a lesser extent, for the eastern part of North America and Europe. Over the ocean, the largest AOD changes correspond to regions with a high concentration of SS aerosols (Fig. S1b), within the tropics and at high latitudes.  $\text{AE}_{550-865}$  is affected by strong changes in the poles, where aerosol concentration is very low, so the global mean values are a bit misleading.  $\text{AE}_{550-865}$  also increases over East Asia, Europe and the eastern part of North America.

#### 4.3.7 Changes in emissions when considering the corrected relative humidity

An additional data assimilation experiment was conducted using the relative humidity from ERA5 (assumed to be the most accurate data available) in order to describe aerosol water uptake. The relative changes in aerosol emissions for this DA experiment ( $\text{DAS}_{\text{ERA5}}$ ) compared with the standard DA experiment ( $\text{DAS}_{\text{ECHAM}}$ ) are depicted in Fig. 13. These changes are quantified by the ratio of  $\text{DAS}_{\text{ERA5}}$  to  $\text{DAS}_{\text{ECHAM}}$ . The evaluations of aerosol optical properties of  $\text{DAS}_{\text{ECHAM}}$  and  $\text{DAS}_{\text{ERA5}}$  against POLDER and AERONET are very similar (not shown), suggesting that the emissions had to change differently in each experiment in order to compensate for the distinct differences in RH that affected aerosol optical properties.

As expected, strong changes occur in the soluble particles, SS and  $\text{SO}_4$ . Overall, both the accumulation and the coarse-mode emissions of SS increase almost everywhere over the ocean. The increase in the accumulation mode is more pronounced in the Southern Hemisphere. The considerable difference between the two DAS experiments is caused by the

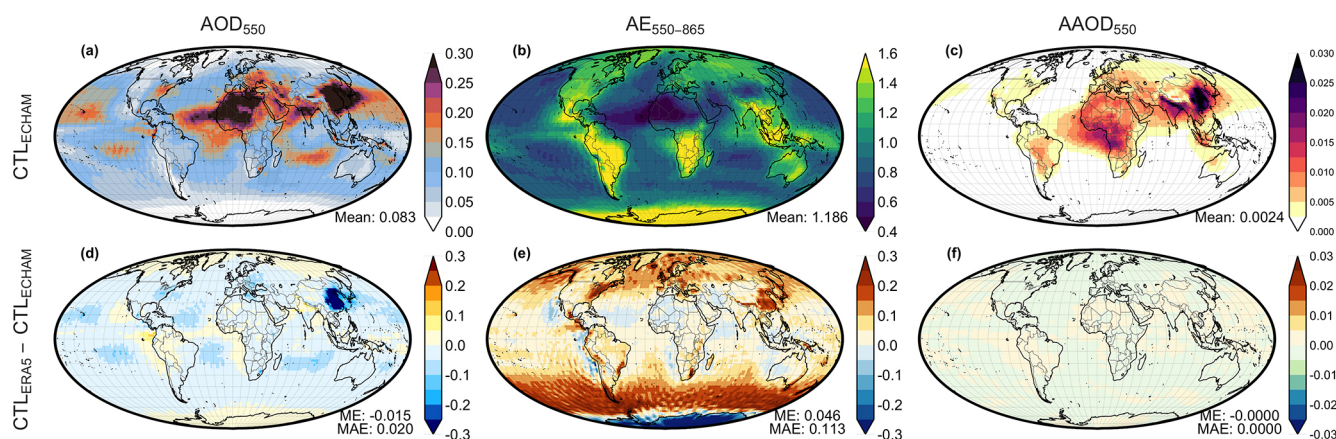


**Figure 12.** Aerosol optical properties of CTL<sub>ECHAM</sub> and the differences between CTL<sub>ERA5</sub> and CTL<sub>ECHAM</sub>.

fact that in DAS<sub>ERA5</sub> aerosol particles are smaller (less water) and hence less efficient in the extinction of light. So, more emissions of more particles are needed to match the measured AOD<sub>550</sub> by POLDER. The global SS emission in the DAS<sub>ERA5</sub> experiment is 2317 Tg yr<sup>-1</sup>.

As for SO<sub>4</sub>, DAS<sub>ERA5</sub> emissions distinctively increase over Southeast Asia by about 2 and to a lesser extent in Europe and North America (Fig. 13g and h). The results over Southeast Asia are particularly interesting, since they could hint at a potential big error in the bottom-up emissions inventories and/or could reveal underlying model errors with different signs that compensate for each other. These changes are discussed in Sect. 4.4.2 using additional evaluations with independent observations. The emission changes in the insoluble species (DU and BC) remain almost unchanged. Additionally, a very small reduction is observed for OC over North America and Southeast Asia, which barely reduces the AOD<sub>550</sub> by about 0.01.

#### 4.3.8 Sulfate emissions in East Asia

In this subsection we use additional observational datasets to evaluate the model over East Asia, and we further investigate the estimated emissions of SO<sub>4</sub> by DAS<sub>ERA5</sub> over Asia. Note that most of the SO<sub>2</sub> sources are in the eastern part of China (Fig. 7h). The emissions of SO<sub>2</sub> and SO<sub>4</sub> for a part of East Asia are depicted in Fig. 14. Additional SO<sub>2</sub> estimates from bottom-up estimates are provided for comparison. DMS emissions are not shown, since they contribute a very small fraction (about 3 %) to the mass production of SO<sub>4</sub> and mostly over the ocean.

The two CTL experiments and DAS<sub>ECHAM</sub> are within the range of previously reported estimates, while the SO<sub>2</sub> and SO<sub>4</sub> emissions in DAS<sub>ERA5</sub> more than doubled compared with CTL<sub>ERA5</sub> (Fig. 14). As already discussed, these large changes are caused by using more accurate relative humidity profiles for aerosol water uptake, which reduce AOD<sub>550</sub> significantly over the area, and, consequently, the emission

estimation system compensates for it by increasing SO<sub>2</sub> and SO<sub>4</sub> emissions. But since the uncertainty in the bottom-up emission inventories is only 5.3 % for eastern China (Chang et al., 2015), it is highly unlikely that DAS<sub>ERA5</sub> emissions are correct.

In Figs. 15 and 16 the CTL<sub>ERA5</sub> and DAS<sub>ERA5</sub> experiments are evaluated against various observations over eastern China. The mean difference in AOD<sub>550</sub> and AE<sub>550-865</sub> against POLDER improves from CTL<sub>ERA5</sub> to DAS<sub>ERA5</sub> (Fig. 15). In addition, the comparison of AOD<sub>550</sub> and AE<sub>550-865</sub> against AERONET improves from CTL<sub>ERA5</sub> to DAS<sub>ERA5</sub> (Fig. 16). Note that AE<sub>550-865</sub> for CTL<sub>ERA5</sub> in Fig. 16h underestimates at low values and overestimates at large values, which compensates for the mean error. The evaluation of surface SO<sub>4</sub> against CAWNET stations (values as reported in X. Y. Zhang et al., 2012) did not provide conclusive evidence for improvement in the DAS<sub>ERA5</sub> experiment, since the mean errors in CTL<sub>ERA5</sub> and DAS<sub>ERA5</sub> are of equal strength with a different sign (Fig. 16i–l).

Although aerosol optical properties are considerably better in DAS<sub>ERA5</sub>, the evaluation of the experiments with the OMI SO<sub>2</sub> column retrievals in Dobson units clearly indicates that the SO<sub>2</sub> amount in DAS<sub>ERA5</sub> is too high compared with OMI. This coincides with the bottom-up emission estimates discussed in Fig. 14. According to these results we conclude that in DAS<sub>ERA5</sub> the SO<sub>2</sub> amount is overestimated, but the SO<sub>4</sub> amount, which is the dominant aerosol type in this region, is consistent with observations (both POLDER and AERONET) of AOD<sub>550</sub> and AE<sub>550-865</sub>.

This inconsistency between SO<sub>2</sub> and SO<sub>4</sub> may be related to errors in the gain and loss mechanisms of SO<sub>4</sub>, which also controls the atmospheric lifetime. Wet deposition is the dominant removal process for SO<sub>4</sub> globally and accounts for 97 % of the total deposition in ECHAM–HAM. On the other hand, wet deposition accounts for only 30 % of the total deposition of SO<sub>2</sub>. Thus, biases in wet deposition will affect the SO<sub>4</sub> lifetime more than the SO<sub>2</sub> lifetime. In ECHAM–HAM

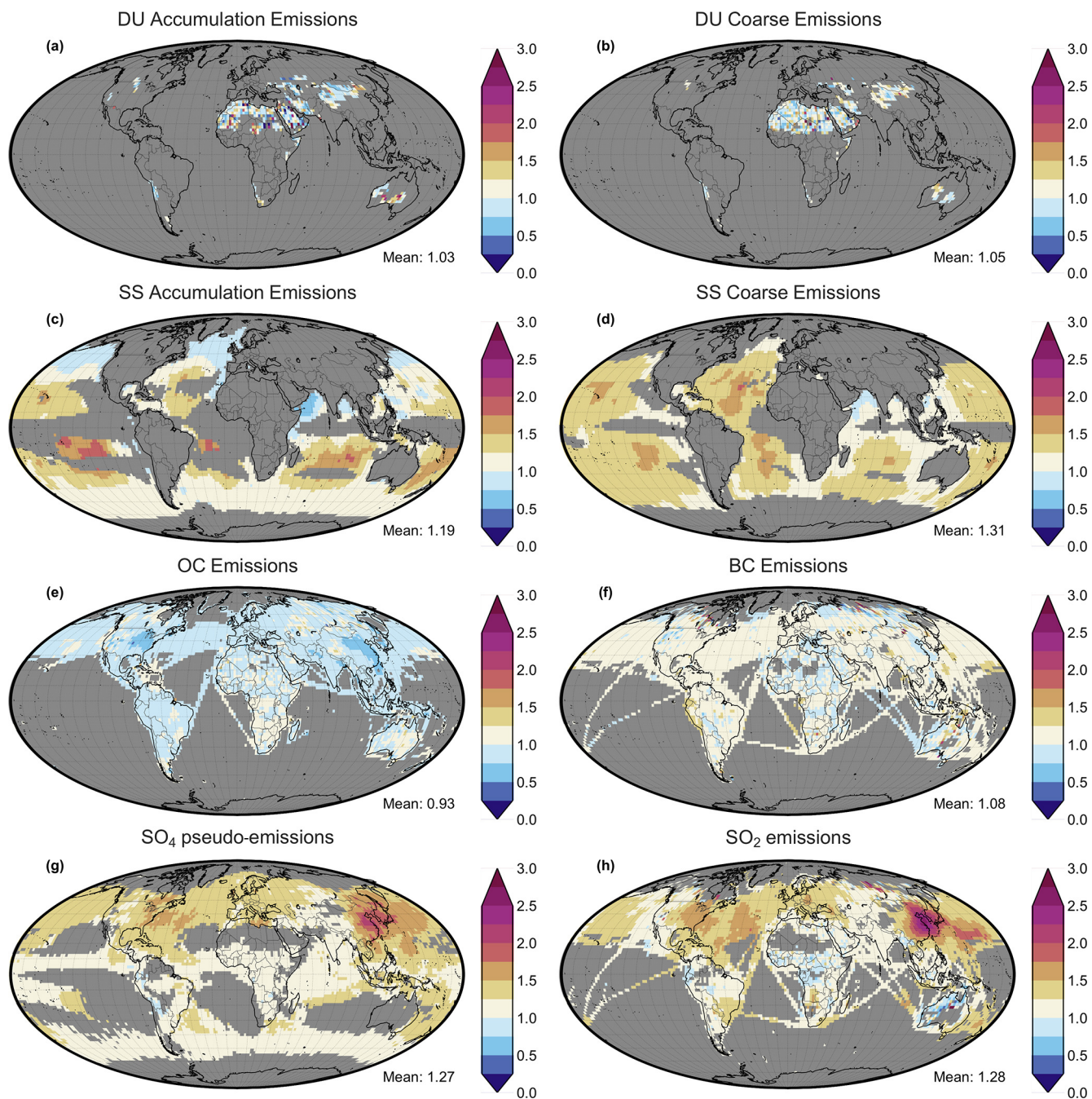


**Figure 13.** Relative changes in aerosol emissions after accounting for the correct relative humidity for aerosol water uptake ( $DAS_{ERA5}$  divided by  $DAS_{ECHAM}$ ) for 2006. The global mean is depicted in the bottom-right corner of each map. Grey grid cells contain emissions lower than the global median value of each species and are excluded from these maps.

wet deposition and specifically below-cloud scavenging simulate the removal rate of aerosol particles because of rain or snow depending on precipitation rate, precipitation area and collection efficiency (K. Zhang et al., 2012). An evaluation with the Global Precipitation Climatology Project (GPCP) version 2.3 shows that both  $CTL_{ERA5}$  and  $DAS_{ERA5}$  overestimate precipitation by more than 50 % over the eastern

China domain (Fig. 15). This overestimation should decrease the modeled atmospheric lifetime of  $SO_4$  and lower the AOD in the area. In order to match observed AOD values, this is compensated for in  $DAS_{ERA5}$  by too high  $SO_2$  and  $SO_4$  emissions.

Globally the total mass production of  $SO_4$  particles in  $ECHAM-HAM$  is mainly driven by oxidation of dissolved

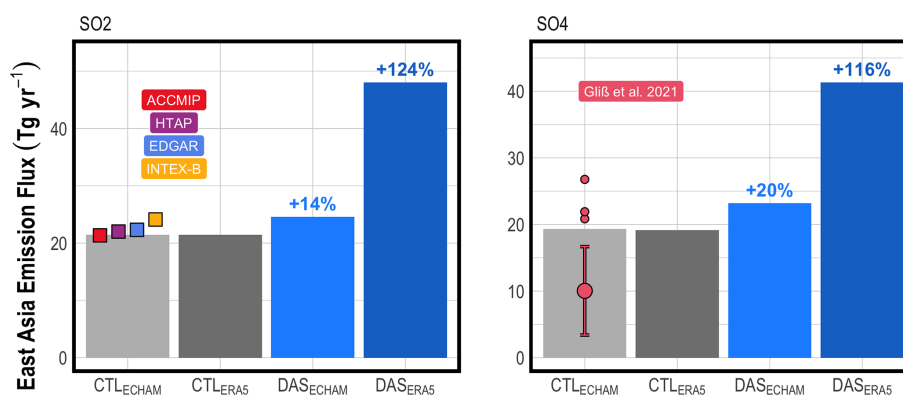


**Figure 14.** Aerosol emissions over China for SO<sub>2</sub> and SO<sub>4</sub> (Tg yr<sup>-1</sup>). The percentage change of the estimated emissions over DAS<sub>ECHAM</sub> and DAS<sub>ERA5</sub> is estimated based on the emissions of CTL<sub>ECHAM</sub> and CTL<sub>ERA5</sub>, respectively. The bars show the sum of the emissions for eastern China (24 to 44° N, 100 to 120° E). The squares depict the annual emissions of 2006 for four bottom-up inventories (ACCMIP, HTAP, EDGAR and INTEX-B) over the same domain as reported in Chang et al. (2015).

SO<sub>2</sub> in clouds by O<sub>3</sub> and H<sub>2</sub>O<sub>2</sub> (72.5 %), followed by an oxidation reaction of OH with SO<sub>2</sub> (20.9 %) and OH with DMS (3.3 %) in cloud-free conditions. Finally, a small percentage is contributed by direct emissions of aerosol SO<sub>4</sub> (2.5 %). Based on MODIS-Terra the cloud liquid water path (LWP) over eastern China is overestimated by more than 50 % in both CTL<sub>ERA5</sub> and DAS<sub>ERA5</sub>, which potentially accelerates the in-cloud production of SO<sub>2</sub> to SO<sub>4</sub> in ECHAM–HAM and inflates the AOD in the area. In an inverse emission estimation like DAS<sub>ERA5</sub>, this would lead to a reduction in SO<sub>2</sub> and SO<sub>4</sub> emissions. The fact that the SO<sub>2</sub> emissions increase to unrealistically large values suggests that errors caused by too strong wet deposition dominate over the error caused by too much in-cloud SO<sub>4</sub> production. A future study with additional sensitivity studies may fully disentangle and quantify the biases of these processes.

Additional causes for the underestimated AOD<sub>550</sub> in CTL<sub>ERA5</sub>, which lead to an excessive increase in SO<sub>2</sub> emissions in DAS<sub>ERA5</sub>, may be the lack of ammonium nitrate (NH<sub>4</sub>NO<sub>3</sub>) in ECHAM–HAM. Particulate nitrates (hereafter referred to as nitrates) form either through aqueous chemical reaction between gaseous ammonia (NH<sub>3</sub>) and gaseous nitric acid (HNO<sub>3</sub>) or through heterogeneous reaction of nitrogen species (e.g., HNO<sub>3</sub>, NO<sub>3</sub> and N<sub>2</sub>O<sub>5</sub>) on the surface of dust and sea salt particles (Bian et al., 2017). Some of the AEROCOM III models that simulate both nitrates and sulfates report that the global mean AOD<sub>550</sub> of sulfates (0.0392) is 5 times greater than the respective global mean AOD<sub>550</sub> of nitrates (0.0072) (Bian et al., 2017). Further, the global contribution of nitrate AOD<sub>550</sub> to the global total AOD<sub>550</sub> according to the ensemble of all AEROCOM III models is about 2 % to 3 % (Gliß et al., 2021). Although the effect of nitrate AOD<sub>550</sub> is limited globally, the effect on a local scale over highly polluted agricultural areas can be considerably higher. According to Park et al. (2014), the nitrate AOD<sub>550</sub> for the year 2006 accounts for more than 15 % of the to-

tal AOD<sub>550</sub> over the East Asia domain and for about 20 % at AERONET sites over the same domain. The AERONET AOD<sub>550</sub> for a similar domain used in Park et al. (2014) is 0.539 (Fig. 16a), from which 0.108 (20 % of 0.539) is contributed by nitrates. Consequently, ECHAM–HAM underestimates AOD<sub>550</sub> by about 0.10 because it does not consider nitrate aerosol.

The missing AOD<sub>550</sub> over East Asia could also be explained if the water uptake process is underestimated in ECHAM–HAM, i.e., if the growth factors at a given relative humidity are underestimated. However, the results in Burgos et al. (2020) do not suggest this because they showed that the ATRAS, CAMS and CAM-OSLO models, which use the  $\kappa$ -Köhler parameterization for aerosol water uptake with very similar kappa values for all aerosol species to ECHAM–HAM, have a good agreement in scattering enhancement factors with 22 different sites (see Burgos et al., 2020, for more details), though with a small positive bias. Thus, the errors in scattering enhancement due to water uptake in ECHAM–HAM are not underestimated and cannot be the cause of the low AOD<sub>550</sub> in CTL<sub>ERA5</sub>.

## 5 Conclusions

We estimated aerosol emissions for the year 2006 based on the assimilation of POLDER observations related to the aerosol amount, size and absorption (AOD<sub>550</sub>, AE<sub>550–865</sub> and SSA<sub>550</sub>). The data assimilation system was developed using an existing ensemble Kalman smoother code (Schutgens et al., 2012) that was modified for the ECHAM–HAM (Tsikerdekis et al., 2022a) model. The global aerosol emissions of all species increase compared with the prior emissions from bottom-up inventories after the assimilation of POLDER observations, in particular 28 % for dust, 75 % for sea salt, 143 % for organic carbon, 75 % for black carbon and 39 % for sulfates. Specifically, the biomass burning emissions of

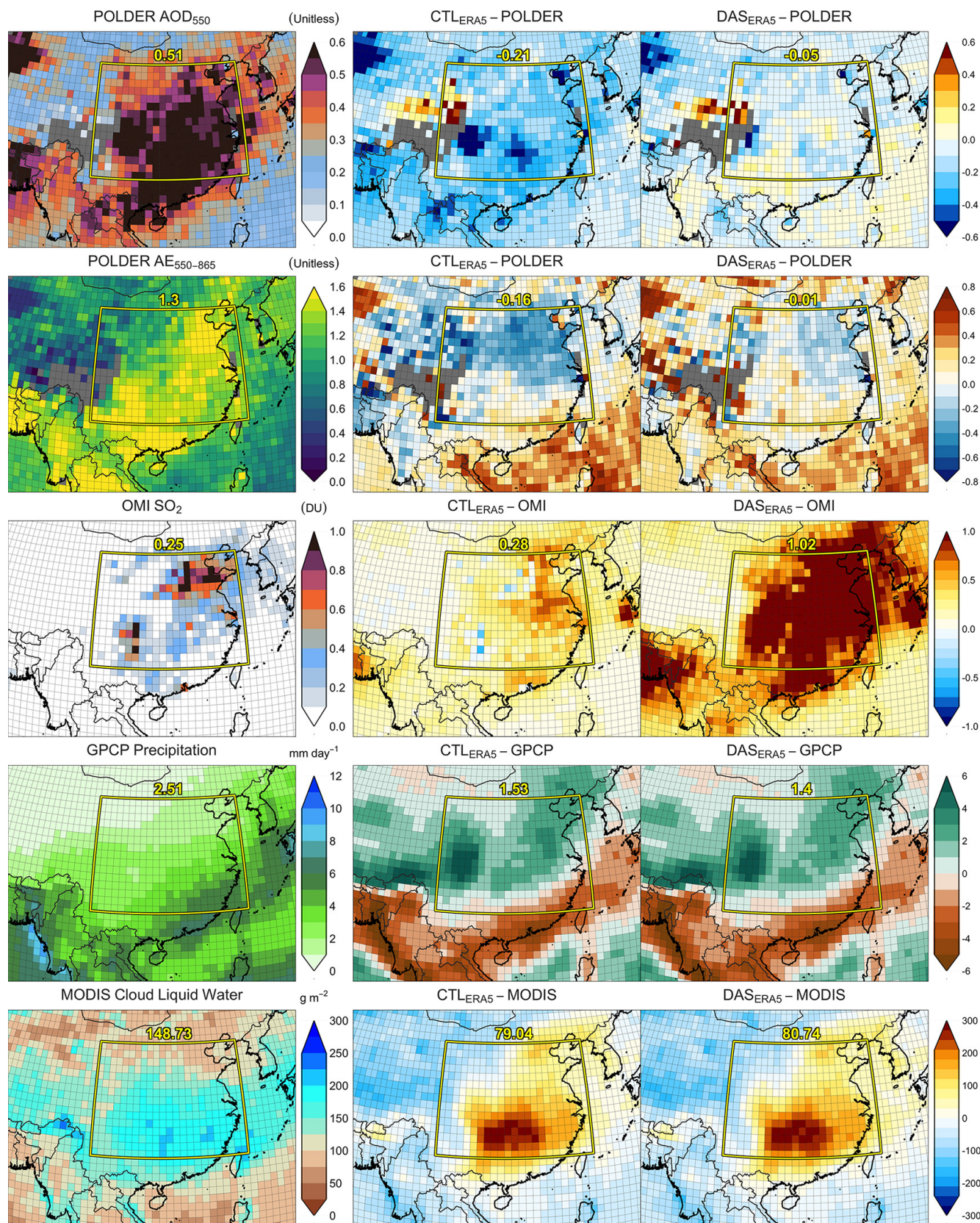


**Figure 15.** The (a) POLDER AOD<sub>550</sub>, (b) POLDER AE<sub>550-865</sub>, (c) OMI SO<sub>2</sub> in Dobson units, (d) GPCP precipitation and (e) MODIS-Terra cloud liquid water over eastern China. The second and third columns show the differences between CTL<sub>ERA5</sub> – observations and DAS<sub>ERA5</sub> – observations, respectively. The number within each figure refers to the mean value of the yellow polygon in each case.

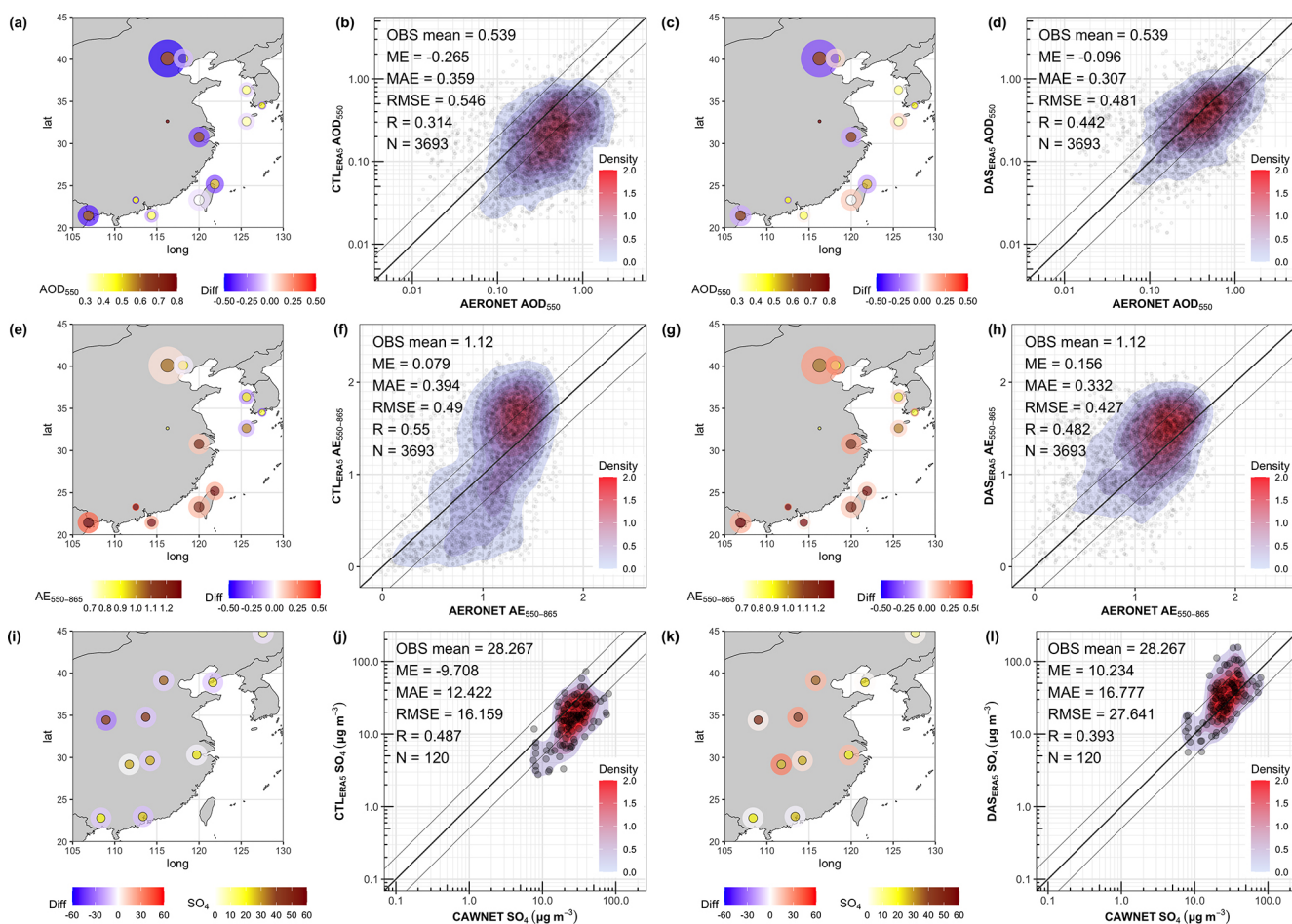


**Figure 16.** An evaluation of the CTL<sub>ERA5</sub> and DAS<sub>ERA5</sub> experiments for AOD<sub>550</sub> and AE<sub>550-865</sub> against AERONET (panels a to h). In the maps the inner circle depicts the mean AE<sub>550-865</sub> of all AERONET stations within a grid cell of the model, while the outer circle depicts the difference between experiments minus AERONET. The size of the points is analogous to the number of the available data points in each case. The scatterplots use all the available data points of the displayed stations. An evaluation of the same two experiments for SO<sub>4</sub> surface concentrations against CAWNET (as reported in X. Y. Zhang et al. (2012) for 2006 and 2007) is shown in panels (i–l).

organic aerosol and black carbon increase by 193 % and 90 %, respectively. The changes lead to a simulated aerosol state that is overall in a better agreement with the assimilated (POLDER) and independent (AERONET and MODIS) observations. However, we found that the global spatial distribution of the AERONET stations cannot fully capture the changes of observables due to the adjusted emissions.

The a priori and estimated emissions are compared with the reported emissions used in the AEROCOM and CMIP5 ensemble of models, as well as other observationally constrained studies. The new dust emissions are very close to the ensemble median of AEROCOM and match the estimated emissions reported by other data assimilation studies quite well (Huneus et al., 2012). However, the addition of a super-coarse mode for dust could increase the modeled dust emissions as well as the estimated dust emissions from our data assimilation system (Kok et al., 2021). New sea salt emissions are close but still on the lower end compared with

the emissions from other studies. A possible explanation is that the ECHAM–HAM sea salt scheme we use (Long et al., 2011) underestimates the coarse sea salt particles, which is characterized by a short lifetime and a small contribution to AOD<sub>550</sub> but has a high impact on the total emissions mass.

The derived organic aerosol emissions are higher than the upper bound of the AEROCOM range, as well as higher than any other top-down estimates. There are four top-down emission estimates (including the present one), and all of them lead to a significant increase compared with the (bottom-up) prior emission (Schutgens et al., 2012; Chen et al., 2019; Huneus et al., 2012). However, the four different estimates span a considerable range, and the estimate of the present work yields the highest emission for organic aerosol. The derived black carbon emissions in this study are closer to the estimated emissions by Chen et al. (2019) and Huneus et al. (2012), and all agree that the emissions should be higher than bottom-up estimates.

In this study we estimate emissions of OC and BC distinctively for biomass burning sources and for all other sources combined. Based on the data assimilation changes we observe in the prior GFAS emissions, we propose scaling factors equal to 2.93 and 1.90 for OC and BC, respectively. Past studies have proposed a scaling factor of 3.4 for GFAS emissions based on AOD (Kaiser et al., 2012; Veira et al., 2015; Tegen et al., 2019). These new scaling factors are based on the assimilation of POLDER observations that include absorption information and could be adopted to future studies to scale the GFAS emissions. It is noted that the absorbing organic aerosol (also known as brown carbon), which strongly absorbs radiation in the ultraviolet wavelengths, is not considered. The OC AAOD contribution to total AAOD in our experiments is about 10 % over the biomass regions in the tropics (South America, Africa and Indonesia), while the rest (90 %) is contributed by BC AAOD. The exclusion of brown carbon may lead to an overestimation of the BC emissions by the data assimilation system, as also discussed in Chen et al. (2019). Brown carbon is a topic of ongoing research, and recent studies have suggested that it may contribute up to 40 % to the total AAOD (Zhang et al., 2021).

We found that estimated sulfate emissions are very sensitive to the relative humidity profile (because of hygroscopic growth) and that ECHAM–HAM significantly overestimates relative humidity. The same holds for virtually all AEROCOM and CMIP6 models. When the aerosol water uptake process in ECHAM–HAM uses the relative humidity of ERA5, the global AOD<sub>550</sub> reduces by 0.015, while the reduction over East Asia can be higher than 0.2. This can be explained by smaller wet growth of aerosols due to lower relative humidity. Thus, we conducted a second yearly data assimilation experiment where new emissions were estimated when the aerosol wet growth in the model uses ERA5 RH (instead of ECHAM–HAM RH). The global emissions of sulfates increased by 85 %, which is considerably higher than the increase in the base experiments. For the same reason, sea salt emissions increased by 123 %. As expected, the emissions of insoluble (dust, black carbon) or not very soluble (organic carbon) species were much less sensitive to the relative humidity.

Specifically, over East Asia, the new emissions of sulfur dioxide (primary precursor for sulfates) more than double in the new setup with ERA5 relative humidity. The new estimates are considerably higher than all the bottom-up emission inventories. A thorough evaluation with independent observations over East Asia reveals that the lack of AOD<sub>550</sub> that leads to an intense increase in sulfur dioxide emissions is possibly caused by (i) the overestimated precipitation that enhances wet deposition and reduces the aerosol lifetime and AOD<sub>550</sub> (ii) or the missing nitrates on ECHAM–HAM that may contribute by up to 15 % of AOD (Park et al., 2014). Conversely, a compensating effect of overestimated cloud liquid water path, which enhances the in-cloud production of SO<sub>4</sub> particles, was also found over the same area, but consid-

ering the lack of AOD<sub>550</sub> this effect is likely less important. A future study should study the gain (e.g., conversion speed of SO<sub>2</sub> to SO<sub>4</sub>) and loss (dry and wet deposition) processes in the model in more detail.

The focus of the present study is to estimate new aerosol emissions based on POLDER, evaluate the results with independent observations, and inter-compare the estimated emissions with prior modeling and data assimilation studies on a yearly basis (Tgyr<sup>-1</sup>). Future studies should also focus on highlighting the daily and monthly variations that top-down techniques can offer as well as on taking advantage of the update-to-date information provided by satellite observations to correct bottom-up emission inventories over regions where emission activity has changed (Elguindi et al., 2020). In addition, our estimated emissions were based on a 2 d time step ( $\Delta T = 2$  d); hence a follow-up study could explore the impact of a lower time step (e.g.,  $\Delta T = 1$  d) on the estimated emissions.

## Appendix A

The uncertainty in POLDER observations is estimated by evaluating it with AERONET for predefined POLDER AOD bins. Uncertainty is defined as the standard deviation of the differences between POLDER and AERONET observations for different POLDER AOD bins. For AOD only, a relative uncertainty was used by dividing by AERONET AOD in each case. Figure A1 depicts the uncertainty in AOD, AE and SSA. Lines illustrate the uncertainty (left axis) and bars the number of paired POLDER and AERONET observations that were used in each AOD<sub>550</sub> bin to estimate the uncertainty (right axis). The AOD<sub>550</sub> relative uncertainty is lower than 50 % for POLDER AOD<sub>550</sub> greater than 0.1, and it steadily decreases both over land and over the ocean as POLDER AOD<sub>550</sub> increases. The land and ocean retrievals are notably different for AE<sub>550–865</sub>, where the mean difference in uncertainty for all AOD<sub>550</sub> bins is 0.466. Thus, it is expected that the over-land AE<sub>550–865</sub> will have little to no effect when assimilated compared with the over-ocean AE<sub>550–865</sub>. Further, we found that over-Sahara AE<sub>550–865</sub> is overestimated by POLDER by 0.524; thus these observations were not used in the assimilation. The uncertainty over land SSA<sub>550</sub> is higher than 0.05 for AOD<sub>550</sub> bins lower than 0.4 and decreases (between 0.04 to 0.02) for AOD<sub>550</sub> higher than 0.4. This strongly suggests that for highly polluted areas, absorption is retrieved by POLDER with reasonable accuracy. The over-ocean SSA<sub>550</sub> uncertainty was estimated only up to the 0.4 AOD<sub>550</sub> bin due to the lack of AERONET observations for higher AODs. Currently a new version of POLDER SRON retrievals is being prepared, which is expected to yield a significantly improved POLDER aerosol product.

In addition to the uncertainty in observations presented in Fig. A1, a representation error was added to the uncertainty



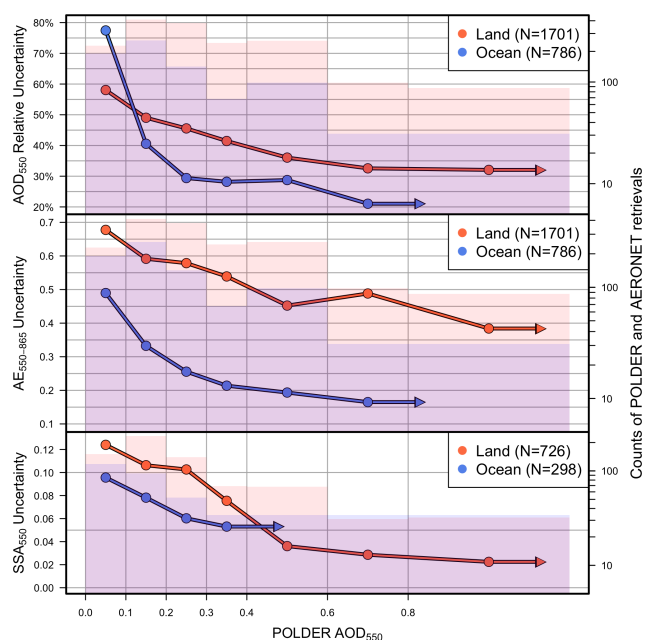


**Figure A1.** POLDER SRON product uncertainty in  $AOD_{550}$ ,  $AE_{550-865}$  and  $SSA_{550}$  based on an AERONET evaluation for several POLDER  $AOD_{550}$  bins. Red and blue lines depict the uncertainty in the over-land and over-ocean retrievals, respectively (left axis). The respective colored bars illustrate the number of collocated POLDER and AERONET retrievals that were used to calculate the observable uncertainty in each  $AOD_{550}$  bin (right axis), and  $N$  depicts the total number. Note that only  $AOD_{550}$  uncertainty was estimated in relative terms, by dividing by AERONET  $AOD_{550}$ . The  $AOD_{550}$  and  $AE_{550-865}$  evaluation is based on the AERONET version 3 level 2.0 direct sun algorithm, while the  $AAOD_{550}$  and  $SSA_{550}$  evaluation is based on the AERONET version 3 level 1.5 direct sun and inversion algorithm.

in  $AOD_{550}$  and  $AE_{550-865}$  observations. Specifically, an analysis was performed using CAMS reanalysis in two resolutions, one in a resolution of  $1^\circ \times 1^\circ$  (resolution of POLDER level 3) and one in a coarser resolution of  $1.875^\circ \times 1.875^\circ$  (resolution of ECHAM–HAM). The objective of this analysis was to determine how well an observation on a  $1^\circ \times 1^\circ$  horizontal resolution represents the respective observations on a  $1.875^\circ \times 1.875^\circ$  model resolution. This was done by firstly collocating the data of the two resolutions. Obviously, each coarse resolution paired with multiple high-resolution observations. For each paired observation the differences were calculated. Then the standard deviation of the differences for each  $1.875^\circ \times 1.875^\circ$  grid box was estimated. The global mean value of all standard deviations was used as a representation error, distinctively for the  $AOD_{550}$  and  $AE_{550-865}$  case. The added representation error for  $AOD_{550}$  is 0.022 and for  $AE_{550-865}$  is 0.062. The respective values for a coarser resolution ( $3.75^\circ \times 3.75^\circ$ ) are 0.045 and 0.120 for  $AOD_{550}$  and  $AE_{550-865}$ , respectively. No representation error was used for the observations of  $SSA_{550}$ , since the SSA was

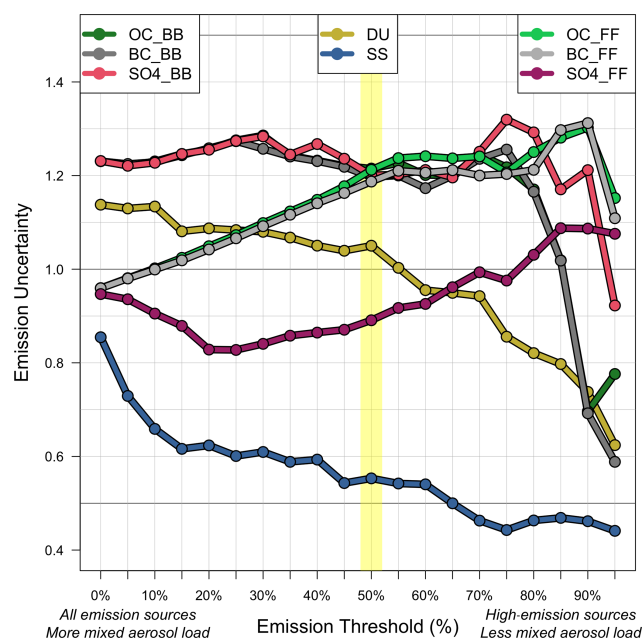


**Figure B1.** The emission uncertainty as a function of the emission threshold for each parameter. The emission uncertainty ( $yy'$  axis) is set as the standard deviation of daily  $AOD_{550}$  differences of POLDER – ECHAM–HAM for the year 2006. The emission threshold ( $xx'$  axis) depicts the percentile of daily emissions. The  $SO_4$  emission uncertainty also represents the emission uncertainty used for  $SO_2$  and DMS. Note that for DU, SS and OC multiple modes are perturbed distinctively, but the modes of those species use the same emission uncertainty. The yellow shaded area highlights the emission uncertainty used in this study, where the emission threshold is set at 50% (includes sources with higher values than the median). For more details, see the text in Appendix B.

not available in the Atmosphere Monitoring Service (ADS) for the CAMS reanalysis.

## Appendix B

The prior emission uncertainties are based on an ensemble of simulations where in each member the emissions of each aerosol species have been distinctively perturbed. The emissions were multiplied with numbers that were sampled from a positive skewed distribution, which had a distinctive standard deviation for each species and a mean of 1. The distinctive standard deviations were based on the standard deviation of the differences between ECHAM–HAM minus POLDER daily AOD. We assumed that the standard deviation of these differences filtered over specific locations can be used as a proxy for emissions uncertainty by species.

In Fig. B1 the estimated emissions uncertainty (standard deviation differences of AOD, explained above) is depicted as a function of several emissions percentiles, where a low percentage contains all the daily grid box emissions and a high percentage contains only the highest daily grid box

emissions. Theoretically, when the emissions threshold is high, the contribution of that specific aerosol species to the total aerosol load in the atmosphere increases; thus the emission uncertainty will be more representative of that species.

The current analysis gives little information on the emissions uncertainty over low-emission sources; thus we assume that low- and high-emission sources share the same uncertainty. The emissions uncertainty for this study was based on the median (50%) emissions threshold in order to filter out cases where multiple aerosol species are mixed in the atmosphere but also to include sources with relative mediocre strength. Note that this approach attributes all modeling errors that may affect aerosol optical properties (e.g., transport, deposition, water uptake, aerosol chemical production) as emissions uncertainty. Consequently, the emissions uncertainty is possibly overestimated in some cases. For example, a previous study has suggested that fossil fuel emissions are lower than 20% for BC and lower than 42% for SO<sub>2</sub> (Granier et al., 2011). Further, note that since we are using AOD as a proxy for emissions uncertainty, the absorbing aerosols (BC) will have a similar uncertainty with the scattering aerosol species (OC) that are emitted in the same locations.

**Data availability.** The model simulations and the assimilated POLDER data are available from Zenodo at the following link: <https://doi.org/10.5281/zenodo.7565093> (Tsikerdekis et al., 2023). The ECHAM–HAM version that was used in this study can be found in the following repository: [https://redmine.hammoz.ethz.ch/projects/hammoz/repository/1/show/echam6-hammoz/branches/uni\\_amsterdam\\_vrije/WC20220422](https://redmine.hammoz.ethz.ch/projects/hammoz/repository/1/show/echam6-hammoz/branches/uni_amsterdam_vrije/WC20220422) (Tsikerdekis et al., 2022b). This repository can be accessed after registration at <https://redmine.hammoz.ethz.ch/projects/hammoz> (Hammoz, 2023). ERA-Interim and ERA5 data are freely available from <https://doi.org/10.24381/cds.bd0915c6> (Hersbach et al., 2018) after registration. The AERONET (<https://aeronet.gsfc.nasa.gov/>, AERONET, 2023) data are freely available.

**Supplement.** The supplement related to this article is available online at: <https://doi.org/10.5194/acp-23-9495-2023-supplement>.

**Author contributions.** AT organized the experiments with the help of OPH and NAJS. AT conducted the experiments and performed the analysis. QZ acquired the AEROCOM III data. AT prepared the paper with contributions from all co-authors.

**Competing interests.** The contact author has declared that none of the authors has any competing interests.

**Disclaimer.** Publisher's note: Copernicus Publications remains neutral with regard to jurisdictional claims in published maps and institutional affiliations.

**Acknowledgements.** We thank the principal investigators as well as the co-investigators and their staff for establishing and maintaining the AERONET sites used in this investigation. This work was carried out on the Dutch National e-Infrastructure with the support of the SURF cooperative.

**Financial support.** This research has been supported by the Nederlandse Organisatie voor Wetenschappelijk Onderzoek (grant no. ALWGO.2017.008).

**Review statement.** This paper was edited by Suvarna Fadnavis and reviewed by two anonymous referees.

## References

- AERONET: Aerosol Robotic Network website, <https://aeronet.gsfc.nasa.gov/>, last access: 24 August 2023.
- Bian, H., Chin, M., Hauglustaine, D. A., Schulz, M., Myhre, G., Bauer, S. E., Lund, M. T., Karydis, V. A., Kucsera, T. L., Pan, X., Pozzer, A., Skeie, R. B., Steenrod, S. D., Sudo, K., Tsigaridis, K., Tsimpidi, A. P., and Tsyro, S. G.: Investigation of global particulate nitrate from the AeroCom phase III experiment, *Atmos. Chem. Phys.*, 17, 12911–12940, <https://doi.org/10.5194/acp-17-12911-2017>, 2017.
- Bruhwyler, L. M. P., Michalak, A. M., Peters, W., Baker, D. F., and Tans, P.: An improved Kalman Smoother for atmospheric inversions, *Atmos. Chem. Phys.*, 5, 2691–2702, <https://doi.org/10.5194/acp-5-2691-2005>, 2005.
- Burgos, M. A., Andrews, E., Titos, G., Benedetti, A., Bian, H., Buchard, V., Curci, G., Kipling, Z., Kirkevåg, A., Kokkola, H., Laakso, A., Letertre-Danczak, J., Lund, M. T., Matsui, H., Myhre, G., Randles, C., Schulz, M., van Noije, T., Zhang, K., Alados-Arboledas, L., Baltensperger, U., Jefferson, A., Sherman, J., Sun, J., Weingartner, E., and Zieger, P.: A global model–measurement evaluation of particle light scattering coefficients at elevated relative humidity, *Atmos. Chem. Phys.*, 20, 10231–10258, <https://doi.org/10.5194/acp-20-10231-2020>, 2020.
- Carter, T. S., Heald, C. L., Jimenez, J. L., Campuzano-Jost, P., Kondo, Y., Moteki, N., Schwarz, J. P., Wiedinmyer, C., Darmenov, A. S., da Silva, A. M., and Kaiser, J. W.: How emissions uncertainty influences the distribution and radiative impacts of smoke from fires in North America, *Atmos. Chem. Phys.*, 20, 2073–2097, <https://doi.org/10.5194/acp-20-2073-2020>, 2020.
- Chang, W., Liao, H., Xin, J., Li, Z., Li, D., and Zhang, X.: Uncertainties in anthropogenic aerosol concentrations and direct radiative forcing induced by emission inventories in eastern China, *Atmos. Res.*, 166, 129–140, <https://doi.org/10.1016/j.atmosres.2015.06.021>, 2015.
- Chen, C., Dubovik, O., Henze, D. K., Lapyonok, T., Chin, M., Ducos, F., Litvinov, P., Huang, X., and Li, L.: Retrieval of desert dust and carbonaceous aerosol emissions over Africa from POLDER/PARASOL products generated by the GRASP algorithm, *Atmos. Chem. Phys.*, 18, 12551–12580, <https://doi.org/10.5194/acp-18-12551-2018>, 2018.
- Chen, C., Dubovik, O., Henze, D. K., Chin, M., Lapyonok, T., Schuster, G. L., Ducos, F., Fuertes, D., Litvinov, P., Li,

- L., Lopatin, A., Hu, Q., and Torres, B.: Constraining global aerosol emissions using POLDER/PARASOL satellite remote sensing observations, *Atmos. Chem. Phys.*, 19, 14585–14606, <https://doi.org/10.5194/acp-19-14585-2019>, 2019.
- Chen, C., Dubovik, O., Schuster, G. L., Chin, M., Henze, D. K., Lapyonok, T., Li, Z., Derimian, Y., and Zhang, Y.: Multi-angular polarimetric remote sensing to pinpoint global aerosol absorption and direct radiative forcing, *Nat. Commun.*, 13, 7459, <https://doi.org/10.1038/s41467-022-35147-y>, 2022.
- Darmenov, A. and da Silva, A.: The quick fire emissions dataset (QFED) – Documentation of versions 2.1, 2.2 and 2.4, NASA/TM-2015-104606, Vol. 38, NASA Global Modeling and Assimilation Office, 183 pp., <https://ntrs.nasa.gov/citations/20180005253> (last access: 24 August 2023), 2015.
- Dubovik, O., Lapyonok, T., Kaufman, Y. J., Chin, M., Ginoux, P., Kahn, R. A., and Sinyuk, A.: Retrieving global aerosol sources from satellites using inverse modeling, *Atmos. Chem. Phys.*, 8, 209–250, <https://doi.org/10.5194/acp-8-209-2008>, 2008.
- Elguindi, N., Granier, C., Stavrou, T., Darras, S., Bauwens, M., Cao, H., Chen, C., van der Gon, H. A. C. D., Dubovik, O., Fu, T. M., Henze, D. K., Jiang, Z., Keita, S., Kuenen, J. J. P., Kurokawa, J., Liousse, C., Miyazaki, K., Müller, J.-F., Qu, Z., Solmon, F., and Zheng, B.: Intercomparison of Magnitudes and Trends in Anthropogenic Surface Emissions From Bottom-Up Inventories, Top-Down Estimates, and Emission Scenarios, *Earth's Future*, 8, e2020EF001520, <https://doi.org/10.1029/2020ef001520>, 2020.
- Escribano, J., Boucher, O., Chevallier, F., and Huneus, N.: Impact of the choice of the satellite aerosol optical depth product in a sub-regional dust emission inversion, *Atmos. Chem. Phys.*, 17, 7111–7126, <https://doi.org/10.5194/acp-17-7111-2017>, 2017.
- Feng, L., Palmer, P. I., Bösch, H., and Dance, S.: Estimating surface CO<sub>2</sub> fluxes from space-borne CO<sub>2</sub> dry air mole fraction observations using an ensemble Kalman Filter, *Atmos. Chem. Phys.*, 9, 2619–2633, <https://doi.org/10.5194/acp-9-2619-2009>, 2009.
- Fu, G. and Hasekamp, O.: Retrieval of aerosol microphysical and optical properties over land using a multimode approach, *Atmos. Meas. Tech.*, 11, 6627–6650, <https://doi.org/10.5194/amt-11-6627-2018>, 2018.
- Fu, G., Hasekamp, O., Rietjens, J., Smit, M., Di Noia, A., Cairns, B., Wasilewski, A., Diner, D., Seidel, F., Xu, F., Knobelspiesse, K., Gao, M., da Silva, A., Burton, S., Hostetler, C., Hair, J., and Ferrare, R.: Aerosol retrievals from different polarimeters during the ACEPOL campaign using a common retrieval algorithm, *Atmos. Meas. Tech.*, 13, 553–573, <https://doi.org/10.5194/amt-13-553-2020>, 2020.
- Glöß, J., Mortier, A., Schulz, M., Andrews, E., Balkanski, Y., Bauer, S. E., Benedictow, A. M. K., Bian, H., Checa-Garcia, R., Chin, M., Ginoux, P., Griesfeller, J. J., Heckel, A., Kipling, Z., Kirkevåg, A., Kokkola, H., Laj, P., Le Sager, P., Lund, M. T., Lund Myhre, C., Matsui, H., Myhre, G., Neubauer, D., van Noije, T., North, P., Olivie, D. J. L., Rémy, S., Sogacheva, L., Takemura, T., Tsigaridis, K., and Tsyro, S. G.: AeroCom phase III multi-model evaluation of the aerosol life cycle and optical properties using ground- and space-based remote sensing as well as surface in situ observations, *Atmos. Chem. Phys.*, 21, 87–128, <https://doi.org/10.5194/acp-21-87-2021>, 2021.
- Granier, C., Bessagnet, B., Bond, T., D'Angiola, A., van der Gon, H. D., Frost, G. J., Heil, A., Kaiser, J. W., Kinne, S., Klimont, Z., Kloster, S., Lamarque, J.-F., Liousse, C., Masui, T., Meleux, F., Mieville, A., Ohara, T., Raut, J.-C., Riahi, K., Schultz, M. G., Smith, S. J., Thompson, A., van Aardenne, J., van der Werf, G. R., and van Vuuren, D. P.: Evolution of anthropogenic and biomass burning emissions of air pollutants at global and regional scales during the 1980–2010 period, *Climatic Change*, 109, 163–190, <https://doi.org/10.1007/s10584-011-0154-1>, 2011.
- Grythe, H., Ström, J., Krejci, R., Quinn, P., and Stohl, A.: A review of sea-spray aerosol source functions using a large global set of sea salt aerosol concentration measurements, *Atmos. Chem. Phys.*, 14, 1277–1297, <https://doi.org/10.5194/acp-14-1277-2014>, 2014.
- Guelle, W., Schulz, M., Balkanski, Y., and Dentener, F.: Influence of the source formulation on modeling the atmospheric global distribution of sea salt aerosol, *J. Geophys. Res.-Atmos.*, 106, 27509–27524, <https://doi.org/10.1029/2001jd900249>, 2001.
- Hammoz: Homepage, <https://redmine.hammoz.ethz.ch/projects/hammoz> (last access: 17 January 2023), 2023.
- Hasekamp, O. P. and Landgraf, J.: Linearization of vector radiative transfer with respect to aerosol properties and its use in satellite remote sensing, *J. Geophys. Res.*, 110, D04203, <https://doi.org/10.1029/2004jd005260>, 2005.
- Hasekamp, O. P. and Landgraf, J.: Linearization of vector radiative transfer by means of the forward-adjoint perturbation theory and its use in atmospheric remote sensing, in: Springer Praxis Books, Springer Berlin Heidelberg, [https://doi.org/10.1007/978-3-540-68435-0\\_5](https://doi.org/10.1007/978-3-540-68435-0_5), pp. 159–204, 2007.
- Hasekamp, O. P., Litvinov, P., and Butz, A.: Aerosol properties over the ocean from PARASOL multiangle photopolarimetric measurements, *J. Geophys. Res.*, 116, D14204, <https://doi.org/10.1029/2010jd015469>, 2011.
- Hasekamp, O. P., Fu, G., Rusli, S. P., Wu, L., Noia, A. D., van de Brugh, J., Landgraf, J., Smit, J. M., Rietjens, J., and van Amerongen, A.: Aerosol measurements by SPeXone on the NASA PACE mission: expected retrieval capabilities, *J. Quant. Spectrosc. Ra.*, 227, 170–184, <https://doi.org/10.1016/j.jqsrt.2019.02.006>, 2019.
- Hersbach, H., Bell, B., Berrisford, P., Biavati, G., Horányi, A., Muñoz Sabater, J., Nicolas, J., Peubey, C., Radu, R., Rozum, I., Schepers, D., Simmons, A., Soci, C., Dee, D., and Thépaut, J.-N.: ERA5 hourly data on pressure levels from 1979 to present, Copernicus Climate Change Service (C3S) Climate Data Store (CDS) [data set], <https://doi.org/10.24381/cds.bd0915c6>, 2018.
- Huneus, N., Schulz, M., Balkanski, Y., Griesfeller, J., Prospero, J., Kinne, S., Bauer, S., Boucher, O., Chin, M., Dentener, F., Diehl, T., Easter, R., Fillmore, D., Ghan, S., Ginoux, P., Grini, A., Horowitz, L., Koch, D., Krol, M. C., Landing, W., Liu, X., Mahowald, N., Miller, R., Morcrette, J.-J., Myhre, G., Penner, J., Perlwitz, J., Stier, P., Takemura, T., and Zender, C. S.: Global dust model intercomparison in AeroCom phase I, *Atmos. Chem. Phys.*, 11, 7781–7816, <https://doi.org/10.5194/acp-11-7781-2011>, 2011.
- Huneus, N., Chevallier, F., and Boucher, O.: Estimating aerosol emissions by assimilating observed aerosol optical depth in a global aerosol model, *Atmos. Chem. Phys.*, 12, 4585–4606, <https://doi.org/10.5194/acp-12-4585-2012>, 2012.
- Hyer, E. J., Reid, J. S., and Zhang, J.: An over-land aerosol optical depth data set for data assimilation by filtering, correction, and aggregation of MODIS Collection 5 optical depth retrievals,

- Atmos. Meas. Tech., 4, 379–408, <https://doi.org/10.5194/amt-4-379-2011>, 2011.
- Ichoku, C. and Ellison, L.: Global top-down smoke-aerosol emissions estimation using satellite fire radiative power measurements, *Atmos. Chem. Phys.*, 14, 6643–6667, <https://doi.org/10.5194/acp-14-6643-2014>, 2014.
- Jin, J., Segers, A., Heemink, A., Yoshida, M., Han, W., and Lin, H.-X.: Dust Emission Inversion Using Himawari-8 AODs Over East Asia: An Extreme Dust Event in May 2017, *J. Adv. Model. Earth Sy.*, 11, 446–467, <https://doi.org/10.1029/2018ms001491>, 2019.
- Kaiser, J. W., Heil, A., Andreae, M. O., Benedetti, A., Chubarova, N., Jones, L., Morcrette, J.-J., Razinger, M., Schultz, M. G., Suttie, M., and van der Werf, G. R.: Biomass burning emissions estimated with a global fire assimilation system based on observed fire radiative power, *Biogeosciences*, 9, 527–554, <https://doi.org/10.5194/bg-9-527-2012>, 2012.
- Kim, D., Chin, M., Yu, H., Diehl, T., Tan, Q., Kahn, R. A., Tsigaridis, K., Bauer, S. E., Takemura, T., Pozzoli, L., Bellouin, N., Schulz, M., Peyridieu, S., Chédin, A., and Koffi, B.: Sources, sinks, and transatlantic transport of North African dust aerosol: A multimodel analysis and comparison with remote sensing data, *J. Geophys. Res.-Atmos.*, 119, 6259–6277, <https://doi.org/10.1002/2013jd021099>, 2014.
- Kinne, S., Schulz, M., Textor, C., Guibert, S., Balkanski, Y., Bauer, S. E., Berntsen, T., Berglen, T. F., Boucher, O., Chin, M., Collins, W., Dentener, F., Diehl, T., Easter, R., Feichter, J., Fillmore, D., Ghan, S., Ginoux, P., Gong, S., Grini, A., Hendricks, J., Herzog, M., Horowitz, L., Isaksen, I., Iversen, T., Kirkevåg, A., Kloster, S., Koch, D., Kristjansson, J. E., Krol, M., Lauer, A., Lamarque, J. F., Lesins, G., Liu, X., Lohmann, U., Montanaro, V., Myhre, G., Penner, J., Pitari, G., Reddy, S., Seland, O., Stier, P., Takemura, T., and Tie, X.: An AeroCom initial assessment – optical properties in aerosol component modules of global models, *Atmos. Chem. Phys.*, 6, 1815–1834, <https://doi.org/10.5194/acp-6-1815-2006>, 2006.
- Kok, J. F., Adebisi, A. A., Albani, S., Balkanski, Y., Checa-Garcia, R., Chin, M., Colarco, P. R., Hamilton, D. S., Huang, Y., Ito, A., Klose, M., Leung, D. M., Li, L., Mahowald, N. M., Miller, R. L., Obiso, V., Pérez García-Pando, C., Rocha-Lima, A., Wan, J. S., and Whicker, C. A.: Improved representation of the global dust cycle using observational constraints on dust properties and abundance, *Atmos. Chem. Phys.*, 21, 8127–8167, <https://doi.org/10.5194/acp-21-8127-2021>, 2021.
- Lacagnina, C., Hasekamp, O. P., Bian, H., Curci, G., Myhre, G., Noije, T., Schulz, M., Skeie, R. B., Takemura, T., and Zhang, K.: Aerosol single-scattering albedo over the global oceans: Comparing PARASOL retrievals with AERONET, OMI, and AeroCom models estimates, *J. Geophys. Res.-Atmos.*, 120, 9814–9836, <https://doi.org/10.1002/2015jd023501>, 2015.
- Lacagnina, C., Hasekamp, O. P., and Torres, O.: Direct radiative effect of aerosols based on PARASOL and OMI satellite observations, *J. Geophys. Res.-Atmos.*, 122, 2366–2388, <https://doi.org/10.1002/2016jd025706>, 2017.
- Laurent, B., Marticorena, B., Bergametti, G., Léon, J. F., and Mahowald, N. M.: Modeling mineral dust emissions from the Sahara desert using new surface properties and soil database, *J. Geophys. Res.*, 113, D14218, <https://doi.org/10.1029/2007jd009484>, 2008.
- Lee, L. A., Pringle, K. J., Reddington, C. L., Mann, G. W., Stier, P., Spracklen, D. V., Pierce, J. R., and Carslaw, K. S.: The magnitude and causes of uncertainty in global model simulations of cloud condensation nuclei, *Atmos. Chem. Phys.*, 13, 8879–8914, <https://doi.org/10.5194/acp-13-8879-2013>, 2013.
- Lewis, E. R., and Schwartz, S. E.: Methods of Determining Size-Dependent Sea Salt Aerosol Production Fluxes, in: *Sea Salt Aerosol Production: Mechanisms, Methods, Measurements and Models*, American Geophysical Union, 152, 101–118, ISBN 9780875904177, 2004.
- Lin, Y.: Humidity variability revealed by a sounding array and its implications for cloud representation in GCMs, *J. Geophys. Res.-Atmos.*, 119, 10499–10514, <https://doi.org/10.1002/2014jd021837>, 2014.
- Long, M. S., Keene, W. C., Kieber, D. J., Erickson, D. J., and Maring, H.: A sea-state based source function for size- and composition-resolved marine aerosol production, *Atmos. Chem. Phys.*, 11, 1203–1216, <https://doi.org/10.5194/acp-11-1203-2011>, 2011.
- Miller, R. L., Cakmur, R. V., Perlwitz, J., Geogdzhayev, I. V., Ginoux, P., Koch, D., Kohfeld, K. E., Prigent, C., Ruedy, R., Schmidt, G. A., and Tegen, I.: Mineral dust aerosols in the NASA Goddard Institute for Space Sciences ModelE atmospheric general circulation model, *J. Geophys. Res.*, 111, D06208, <https://doi.org/10.1029/2005jd005796>, 2006.
- Mishchenko, M. I. and Travis, L. D.: Satellite retrieval of aerosol properties over the ocean using polarization as well as intensity of reflected sunlight, *J. Geophys. Res.-Atmos.*, 102, 16989–17013, <https://doi.org/10.1029/96jd02425>, 1997.
- Myhre, G., Samset, B. H., Schulz, M., Balkanski, Y., Bauer, S., Berntsen, T. K., Bian, H., Bellouin, N., Chin, M., Diehl, T., Easter, R. C., Feichter, J., Ghan, S. J., Hauglustaine, D., Iversen, T., Kinne, S., Kirkevåg, A., Lamarque, J.-F., Lin, G., Liu, X., Lund, M. T., Luo, G., Ma, X., van Noije, T., Penner, J. E., Rasch, P. J., Ruiz, A., Seland, Ø., Skeie, R. B., Stier, P., Takemura, T., Tsigaridis, K., Wang, P., Wang, Z., Xu, L., Yu, H., Yu, F., Yoon, J.-H., Zhang, K., Zhang, H., and Zhou, C.: Radiative forcing of the direct aerosol effect from AeroCom Phase II simulations, *Atmos. Chem. Phys.*, 13, 1853–1877, <https://doi.org/10.5194/acp-13-1853-2013>, 2013.
- O'Donnell, D., Tsigaridis, K., and Feichter, J.: Estimating the direct and indirect effects of secondary organic aerosols using ECHAM5-HAM, *Atmos. Chem. Phys.*, 11, 8635–8659, <https://doi.org/10.5194/acp-11-8635-2011>, 2011.
- Pan, X., Ichoku, C., Chin, M., Bian, H., Darmenov, A., Colarco, P., Ellison, L., Kucsera, T., da Silva, A., Wang, J., Oda, T., and Cui, G.: Six global biomass burning emission datasets: intercomparison and application in one global aerosol model, *Atmos. Chem. Phys.*, 20, 969–994, <https://doi.org/10.5194/acp-20-969-2020>, 2020.
- Park, R. S., Lee, S., Shin, S.-K., and Song, C. H.: Contribution of ammonium nitrate to aerosol optical depth and direct radiative forcing by aerosols over East Asia, *Atmos. Chem. Phys.*, 14, 2185–2201, <https://doi.org/10.5194/acp-14-2185-2014>, 2014.
- Peters, W., Miller, J. B., Whitaker, J., Denning, A. S., Hirsch, A., Krol, M. C., Zupanski, D., Bruhwiler, L., and Tans, P. P.: An ensemble data assimilation system to estimate CO<sub>2</sub> surface fluxes from atmospheric trace gas observations, *J. Geophys. Res.*, 110, D24304, <https://doi.org/10.1029/2005jd006157>, 2005.

- Petters, M. D. and Kreidenweis, S. M.: A single parameter representation of hygroscopic growth and cloud condensation nucleus activity, *Atmos. Chem. Phys.*, 7, 1961–1971, <https://doi.org/10.5194/acp-7-1961-2007>, 2007.
- Petters, M. D. and Kreidenweis, S. M.: A single parameter representation of hygroscopic growth and cloud condensation nucleus activity – Part 3: Including surfactant partitioning, *Atmos. Chem. Phys.*, 13, 1081–1091, <https://doi.org/10.5194/acp-13-1081-2013>, 2013.
- Pope, R. J., Marsham, J. H., Knippertz, P., Brooks, M. E., and Roberts, A. J.: Identifying errors in dust models from data assimilation, *Geophys. Res. Lett.*, 43, 9270–9279, <https://doi.org/10.1002/2016gl070621>, 2016.
- Saikawa, E., Kim, H., Zhong, M., Avramov, A., Zhao, Y., Janssens-Maenhout, G., Kurokawa, J.-I., Klimont, Z., Wagner, F., Naik, V., Horowitz, L. W., and Zhang, Q.: Comparison of emissions inventories of anthropogenic air pollutants and greenhouse gases in China, *Atmos. Chem. Phys.*, 17, 6393–6421, <https://doi.org/10.5194/acp-17-6393-2017>, 2017.
- Sayer, A. M., Munchak, L. A., Hsu, N. C., Levy, R. C., Bettenhausen, C., and Jeong, M.-J.: MODIS Collection 6 aerosol products: Comparison between Aqua’s e-Deep Blue, Dark Target, and “merged” data sets, and usage recommendations, *J. Geophys. Res.-Atmos.*, 119, 13965–13989, <https://doi.org/10.1002/2014JD022453>, 2014.
- Schepers, D., van de Brugh, J., Hahne, P., Butz, A., Hasekamp, O., and Landgraf, J.: LINTRAN v2.0: A linearised vector radiative transfer model for efficient simulation of satellite-borne nadir-viewing reflection measurements of cloudy atmospheres, *J. Quant. Spectrosc. Ra.*, 149, 347–359, <https://doi.org/10.1016/j.jqsrt.2014.08.019>, 2014.
- Schultz, M. G., Stadler, S., Schröder, S., Taraborrelli, D., Franco, B., Krefting, J., Henrot, A., Ferrachat, S., Lohmann, U., Neubauer, D., Siegenthaler-Le Drian, C., Wahl, S., Kokkola, H., Kühn, T., Rast, S., Schmidt, H., Stier, P., Kinnison, D., Tyndall, G. S., Orlando, J. J., and Wespes, C.: The chemistry–climate model ECHAM6.3-HAM2.3-MOZ1.0, *Geosci. Model Dev.*, 11, 1695–1723, <https://doi.org/10.5194/gmd-11-1695-2018>, 2018.
- Schutgens, N., Nakata, M., and Nakajima, T.: Estimating Aerosol Emissions by Assimilating Remote Sensing Observations into a Global Transport Model, *Remote Sens.-Basel*, 4, 3528–3543, <https://doi.org/10.3390/rs4113528>, 2012.
- Schutgens, N., Sayer, A. M., Heckel, A., Hsu, C., Jethva, H., de Leeuw, G., Leonard, P. J. T., Levy, R. C., Lipponen, A., Lyapustin, A., North, P., Popp, T., Poulsen, C., Sawyer, V., Sogacheva, L., Thomas, G., Torres, O., Wang, Y., Kinne, S., Schulz, M., and Stier, P.: An AeroCom–AeroSat study: intercomparison of satellite AOD datasets for aerosol model evaluation, *Atmos. Chem. Phys.*, 20, 12431–12457, <https://doi.org/10.5194/acp-20-12431-2020>, 2020.
- Schutgens, N., Dubovik, O., Hasekamp, O., Torres, O., Jethva, H., Leonard, P. J. T., Litvinov, P., Redemann, J., Shinozuka, Y., de Leeuw, G., Kinne, S., Popp, T., Schulz, M., and Stier, P.: AEROCOM and AEROSAT AAOD and SSA study – Part 1: Evaluation and intercomparison of satellite measurements, *Atmos. Chem. Phys.*, 21, 6895–6917, <https://doi.org/10.5194/acp-21-6895-2021>, 2021.
- Schutgens, N. A. J. and Stier, P.: A pathway analysis of global aerosol processes, *Atmos. Chem. Phys.*, 14, 11657–11686, <https://doi.org/10.5194/acp-14-11657-2014>, 2014.
- Sekiyama, T. T., Tanaka, T. Y., Shimizu, A., and Miyoshi, T.: Data assimilation of CALIPSO aerosol observations, *Atmos. Chem. Phys.*, 10, 39–49, <https://doi.org/10.5194/acp-10-39-2010>, 2010.
- Shi, Y., Zhang, J., Reid, J. S., Hyer, E. J., Eck, T. F., Holben, B. N., and Kahn, R. A.: A critical examination of spatial biases between MODIS and MISR aerosol products – application for potential AERONET deployment, *Atmos. Meas. Tech.*, 4, 2823–2836, <https://doi.org/10.5194/amt-4-2823-2011>, 2011.
- Stap, F. A., Hasekamp, O. P., and Röckmann, T.: Sensitivity of PARASOL multi-angle photopolarimetric aerosol retrievals to cloud contamination, *Atmos. Meas. Tech.*, 8, 1287–1301, <https://doi.org/10.5194/amt-8-1287-2015>, 2015.
- Stevens, B., Giorgetta, M., Esch, M., Mauritsen, T., Crueger, T., Rast, S., Salzmann, M., Schmidt, H., Bader, J., Block, K., Brokopf, R., Fast, I., Kinne, S., Kornblüeh, L., Lohmann, U., Pincus, R., Reichler, T., and Roeckner, E.: Atmospheric component of the MPI-M Earth System Model: ECHAM6, *J. Adv. Model. Earth Sy.*, 5, 146–172, <https://doi.org/10.1002/jame.20015>, 2013.
- Stier, P., Feichter, J., Kinne, S., Kloster, S., Vignati, E., Wilson, J., Ganzeveld, L., Tegen, I., Werner, M., Balkanski, Y., Schulz, M., Boucher, O., Minikin, A., and Petzold, A.: The aerosol-climate model ECHAM5-HAM, *Atmos. Chem. Phys.*, 5, 1125–1156, <https://doi.org/10.5194/acp-5-1125-2005>, 2005.
- Tegen, I., Harrison, S. P., Kohfeld, K., Prentice, I. C., Coe, M., and Heimann, M.: Impact of vegetation and preferential source areas on global dust aerosol: Results from a model study, *J. Geophys. Res.-Atmos.*, 107, AAC 14-1–AAC 14-27, <https://doi.org/10.1029/2001jd000963>, 2002.
- Tegen, I., Neubauer, D., Ferrachat, S., Siegenthaler-Le Drian, C., Bey, I., Schutgens, N., Stier, P., Watson-Parris, D., Stanelle, T., Schmidt, H., Rast, S., Kokkola, H., Schultz, M., Schroeder, S., Daskalakis, N., Barthel, S., Heinold, B., and Lohmann, U.: The global aerosol–climate model ECHAM6.3–HAM2.3 – Part 1: Aerosol evaluation, *Geosci. Model Dev.*, 12, 1643–1677, <https://doi.org/10.5194/gmd-12-1643-2019>, 2019.
- Textor, C., Schulz, M., Guibert, S., Kinne, S., Balkanski, Y., Bauer, S., Bernsten, T., Berglen, T., Boucher, O., Chin, M., Dentener, F., Diehl, T., Easter, R., Feichter, H., Fillmore, D., Ghan, S., Ginoux, P., Gong, S., Grini, A., Hendricks, J., Horowitz, L., Huang, P., Isaksen, I., Iversen, I., Kloster, S., Koch, D., Kirkevåg, A., Kristjansson, J. E., Krol, M., Lauer, A., Lamarque, J. F., Liu, X., Montanaro, V., Myhre, G., Penner, J., Pitari, G., Reddy, S., Seland, Ø., Stier, P., Takemura, T., and Tie, X.: Analysis and quantification of the diversities of aerosol life cycles within AeroCom, *Atmos. Chem. Phys.*, 6, 1777–1813, <https://doi.org/10.5194/acp-6-1777-2006>, 2006.
- Textor, C., Schulz, M., Guibert, S., Kinne, S., Balkanski, Y., Bauer, S., Bernsten, T., Berglen, T., Boucher, O., Chin, M., Dentener, F., Diehl, T., Feichter, J., Fillmore, D., Ginoux, P., Gong, S., Grini, A., Hendricks, J., Horowitz, L., Huang, P., Isaksen, I. S. A., Iversen, T., Kloster, S., Koch, D., Kirkevåg, A., Kristjansson, J. E., Krol, M., Lauer, A., Lamarque, J. F., Liu, X., Montanaro, V., Myhre, G., Penner, J. E., Pitari, G., Reddy, M. S., Seland, Ø., Stier, P., Takemura, T., and Tie, X.: The effect of harmonized emissions on aerosol properties in global models –

- an AeroCom experiment, *Atmos. Chem. Phys.*, 7, 4489–4501, <https://doi.org/10.5194/acp-7-4489-2007>, 2007.
- Tian, B., Fetzer, E. J., Kahn, B. H., Teixeira, J., Manning, E., and Hearty, T.: Evaluating CMIP5 models using AIRS tropospheric air temperature and specific humidity climatology, *J. Geophys. Res.-Atmos.*, 118, 114–134, <https://doi.org/10.1029/2012jd018607>, 2013.
- Tsikerdekis, A., Schutgens, N. A. J., and Hasekamp, O. P.: Assimilating aerosol optical properties related to size and absorption from POLDER/PARASOL with an ensemble data assimilation system, *Atmos. Chem. Phys.*, 21, 2637–2674, <https://doi.org/10.5194/acp-21-2637-2021>, 2021.
- Tsikerdekis, A., Schutgens, N. A. J., Fu, G., and Hasekamp, O. P.: Estimating aerosol emission from SPEXone on the NASA PACE mission using an ensemble Kalman smoother: observing system simulation experiments (OSSEs), *Geosci. Model Dev.*, 15, 3253–3279, <https://doi.org/10.5194/gmd-15-3253-2022>, 2022a.
- Tsikerdekis, A., Hasekamp, O. P., Schutgens, N. A. J., and Qirui Zhong: ECHAM-HAM version for the manuscript: Aerosol emissions estimation with POLDER, [https://redmine.hammoz.ethz.ch/projects/hammoz/repository/1/show/echam6-hammoz/branches/uni\\_amsterdam\\_vrije/WC20220422](https://redmine.hammoz.ethz.ch/projects/hammoz/repository/1/show/echam6-hammoz/branches/uni_amsterdam_vrije/WC20220422) (last access: 24 August 2023), 2022b.
- Tsikerdekis, A., Hasekamp, O. P., Schutgens, N. A. J., and Zhong, Q.: Data for the manuscript: Aerosol emissions estimation with POLDER, Zenodo [data set], <https://doi.org/10.5281/zenodo.7565093>, 2023.
- van der Werf, G. R., Randerson, J. T., Giglio, L., van Leeuwen, T. T., Chen, Y., Rogers, B. M., Mu, M., van Marle, M. J. E., Morton, D. C., Collatz, G. J., Yokelson, R. J., and Kasibhatla, P. S.: Global fire emissions estimates during 1997–2016, *Earth Syst. Sci. Data*, 9, 697–720, <https://doi.org/10.5194/essd-9-697-2017>, 2017.
- Veira, A., Kloster, S., Schutgens, N. A. J., and Kaiser, J. W.: Fire emission heights in the climate system – Part 2: Impact on transport, black carbon concentrations and radiation, *Atmos. Chem. Phys.*, 15, 7173–7193, <https://doi.org/10.5194/acp-15-7173-2015>, 2015.
- Vignati, E., Wilson, J., and Stier, P.: M7: An efficient size-resolved aerosol microphysics module for large-scale aerosol transport models, *J. Geophys. Res.-Atmos.*, 109, D22202, <https://doi.org/10.1029/2003jd004485>, 2004.
- Wiedinmyer, C., Akagi, S. K., Yokelson, R. J., Emmons, L. K., Al-Saadi, J. A., Orlando, J. J., and Soja, A. J.: The Fire INventory from NCAR (FINN): a high resolution global model to estimate the emissions from open burning, *Geosci. Model Dev.*, 4, 625–641, <https://doi.org/10.5194/gmd-4-625-2011>, 2011.
- Wu, C., Lin, Z., and Liu, X.: The global dust cycle and uncertainty in CMIP5 (Coupled Model Intercomparison Project phase 5) models, *Atmos. Chem. Phys.*, 20, 10401–10425, <https://doi.org/10.5194/acp-20-10401-2020>, 2020.
- Wu, L., Hasekamp, O., van Diedenhoven, B., and Cairns, B.: Aerosol retrieval from multiangle, multispectral photopolarimetric measurements: importance of spectral range and angular resolution, *Atmos. Meas. Tech.*, 8, 2625–2638, <https://doi.org/10.5194/amt-8-2625-2015>, 2015.
- Xu, X., Wang, J., Henze, D. K., Qu, W., and Kopacz, M.: Constraints on aerosol sources using GEOS-Chem adjoint and MODIS110 radiances, and evaluation with multisensor (OMI, MISR) data, *J. Geophys. Res.-Atmos.*, 118, 6396–6413, <https://doi.org/10.1002/jgrd.50515>, 2013.
- Xu, Z., Han, Y., Tam, C.-Y., Yang, Z.-L., and Fu, C.: Bias-corrected CMIP6 global dataset for dynamical downscaling of the historical and future climate (1979–2100), *Scientific Data*, 8, 293, <https://doi.org/10.1038/s41597-021-01079-3>, 2021.
- Yoshioka, M., Regayre, L. A., Pringle, K. J., Johnson, J. S., Mann, G. W., Partridge, D. G., Sexton, D. M. H., Lister, G. M. S., Schutgens, N., Stier, P., Kipling, Z., Bellouin, N., Browse, J., Booth, B. B. B., Johnson, C. E., Johnson, B., Mollard, J. D. P., Lee, L., and Carslaw, K. S.: Ensembles of Global Climate Model Variants Designed for the Quantification and Constraint of Uncertainty in Aerosols and Their Radiative Forcing, *J. Adv. Model. Earth Sy.*, 11, 3728–3754, <https://doi.org/10.1029/2019ms001628>, 2019.
- Zhang, J. and Reid, J. S.: MODIS aerosol product analysis for data assimilation: Assessment of over-ocean level 2 aerosol optical thickness retrievals, *J. Geophys. Res.*, 111, D22207, <https://doi.org/10.1029/2005jd006898>, 2006.
- Zhang, K., O'Donnell, D., Kazil, J., Stier, P., Kinne, S., Lohmann, U., Ferrachat, S., Croft, B., Quaas, J., Wan, H., Rast, S., and Feichter, J.: The global aerosol-climate model ECHAM-HAM, version 2: sensitivity to improvements in process representations, *Atmos. Chem. Phys.*, 12, 8911–8949, <https://doi.org/10.5194/acp-12-8911-2012>, 2012.
- Zhang, L., Henze, D. K., Grell, G. A., Carmichael, G. R., Bousserrez, N., Zhang, Q., Torres, O., Ahn, C., Lu, Z., Cao, J., and Mao, Y.: Constraining black carbon aerosol over Asia using OMI absorption optical depth and the adjoint of GEOS-Chem, *Atmos. Chem. Phys.*, 15, 10281–10308, <https://doi.org/10.5194/acp-15-10281-2015>, 2015.
- Zhang, Q., Streets, D. G., Carmichael, G. R., He, K. B., Huo, H., Kannari, A., Klimont, Z., Park, I. S., Reddy, S., Fu, J. S., Chen, D., Duan, L., Lei, Y., Wang, L. T., and Yao, Z. L.: Asian emissions in 2006 for the NASA INTEX-B mission, *Atmos. Chem. Phys.*, 9, 5131–5153, <https://doi.org/10.5194/acp-9-5131-2009>, 2009.
- Zhang, X. Y., Wang, Y. Q., Niu, T., Zhang, X. C., Gong, S. L., Zhang, Y. M., and Sun, J. Y.: Atmospheric aerosol compositions in China: spatial/temporal variability, chemical signature, regional haze distribution and comparisons with global aerosols, *Atmos. Chem. Phys.*, 12, 779–799, <https://doi.org/10.5194/acp-12-779-2012>, 2012.
- Zhang, Y., Peng, Y., Song, W., Zhang, Y.-L., Ponsawansong, P., Prapamontol, T., and Wang, Y.: Contribution of brown carbon to the light absorption and radiative effect of carbonaceous aerosols from biomass burning emissions in Chiang Mai, Thailand, *Atmos. Environ.*, 260, 118–144, <https://doi.org/10.1016/j.atmosenv.2021.118544>, 2021.
- Zhong, Q., Schutgens, N., van der Werf, G., van Noije, T., Tsigaridis, K., Bauer, S. E., Mielonen, T., Kirkevåg, A., Seland, Ø., Kokkola, H., Checa-Garcia, R., Neubauer, D., Kipling, Z., Matsui, H., Ginoux, P., Takemura, T., Le Sager, P., Rémy, S., Bian, H., Chin, M., Zhang, K., Zhu, J., Tsyro, S. G., Curci, G., Protonotariou, A., Johnson, B., Penner, J. E., Bellouin, N., Skeie, R. B., and Myhre, G.: Satellite-based evaluation of AeroCom model bias in biomass burning regions, *Atmos. Chem. Phys.*, 22, 11009–11032, <https://doi.org/10.5194/acp-22-11009-2022>, 2022.